

AD-A261 129

2



SAR-RELATED STRESS VARIABILITY IN THE
MARINE ATMOSPHERIC BOUNDARY LAYER (MABL)

Grant Number N00014-90-J-4012

June 1, 1990 – September 30, 1992

Final Report

Hampton N. Shirer
George S. Young
Department of Meteorology
The Pennsylvania State University

SDTIC
ELECTE
FEB 08 1993
S E D

DISTRIBUTION STATEMENT
Approved for public release
Distribution Unlimited

A High-Res ARI Study

The Office of Naval Research
Ocean Engineering Division (Remote Sensing)

93 1 22 041

93-01153



Table of Contents

1. Introduction 1

2. Observations during the first High-Res cruise 2

3. Modeling of submesoscale BL structures 5

4. Analysis of BL observations 7

5. An improved correlation dimension algorithm 9

References 10

Publications, Presentations, and Reports 13

Personnel Funded 15

Appendix A (Sikora and Young, 1993) 16

Appendix B (Wells *et al.*, 1993) 48

Accession For	
NTIS CRA&I	<input checked="" type="checkbox"/>
DTIC TAB	<input type="checkbox"/>
Unannounced	<input type="checkbox"/>
Justification	
By	
Distribution /	
Availability Codes	
Dist	Avail and/or Special
A-1	

DTIC QUALITY INSPECTED 1

Statement A per telecon
 Dr. Dennis Trizna ONR/Code 1121
 Arlington, VA 22217-5000

NW 2/1/93

1. Introduction

Satellite- or aircraft-borne synthetic aperture radars (SAR) have the potential to serve as a powerful and essential part of the global meteorological/oceanographic observation system (Visecky and Stewart, 1982; Phillips, 1988; NASA, 1988). While the potential of SAR systems is enormous, quantitative interpretation of SAR signals has clearly been frustrated by our incomplete understanding of the relationships between the radar backscatter cross section σ^0 and a complicated heterogeneous and constantly changing state of the sea surface.

One analytical approach (Alpers *et al.*, 1981) is to describe σ^0 in terms of a modulation transfer function $R(\mathbf{K})$, in which R is a function of wave tilt as well as hydrodynamic and orbital velocity effects. It is important to note, however, that each of these effects also depends in a complicated fashion upon the structure of the overlying marine atmospheric boundary layer (MABL). The use of empirical relationships such as the "SASS-1 power law model" has led to considerable uncertainty because the fundamental relationships are circumstantially rather than physically or mathematically defined. The combination of wave-current interaction models with physically based radar scattering models is being used by other High-Res Accelerated Research Initiative (ARI) Principal Investigators to address these problems. Because the dominant atmospheric forcing of the sea surface is caused by wind stress, much better knowledge of the spatial and temporal variability of this stress is required before the wave-action spectrum can be adequately specified by such wave-current interaction models.

In the first phase of our High-Res ARI work summarized here, we began developing two new marine atmospheric boundary layer models of the surface stress caused by submesoscale boundary layer coherent structures and we finished obtaining planview patterns of surface stress variability caused by MABL updrafts and downdrafts (Sikora, 1992; Sikora and Young, 1992, 1993). As a result of observations taken in September, 1991 during the High-Res ARI pilot cruise in Gulf Stream current, we began turning our attention to such mesoscale atmospheric circulations as the solenoidal circulation over the sea surface temperature front, the coastal sea breeze circulation, and the flow between the Bermuda High and the diurnally varying pressure trough on the coastal plain. These phenomena are expected to occur again during the second ARI cruise in the summer of 1993.

The submesoscale convective structures of importance include horizontal roll vortices, which are quasi-two-dimensional circulations that fill the boundary layer (BL), and BL convective cells, which are fully three-dimensional flows that may replace the rolls as the surface energy fluxes increase, or which may form independently of the rolls in less windy conditions. Each of these circulations depends sensitively and to varying degrees upon different dynamical and thermodynamical forcing mechanisms; important ones include BL wind shear, air/sea temperature difference, and the magnitude of radiational and latent heating in clouds. All of these mechanisms contribute to the transport of horizontal momentum downward and so to stress variability at the sea surface. The

horizontal scales of this contribution to the total stress are the same—about 100 m to 10 km—as that of the circulations themselves. Evidence from SAR imagery of significant stress variations caused by two-dimensional BL roll vortices can be plausibly inferred from Fig. 19 of Visecky and Stewart (1982) and is very convincingly found in the pass 1339 SEASAT dataset by Gerling (1985, 1986). Moreover, three-dimensional convective cells are evidenced in the orbit 832 ERS-1 SAR image obtained by Dr. Bob Beal of The Johns Hopkins University Applied Research Laboratory (APL); this image is centered on the coordinates $36^{\circ} 24' N$, $74^{\circ} 00' W$ and was taken on 13 September 1991 at 0321 Z during the first High-Res cruise. Such submesoscale, two- and three-dimensional structures, which are quite common over the Gulf Stream, are expected to be seen during the 1993 High-Res field program as well.

In this report, we briefly review our progress on the work that will be continued and extended during the second phase of the project from October 1, 1992 to September 30, 1995. In Appendix A and Appendix B we give two manuscripts of journal articles summarizing our results. The first one by Sikora and Young (1993) discusses the planview patterns of surface stress variability and will appear in *Boundary Layer Meteorology*, while the second one by Wells *et al.* (1993) discusses a new method for estimating the correlation dimension of boundary layer turbulent time series.

2. Observations during the first High-Res cruise

Instrumentation for monitoring the surface fluxes of momentum, heat, moisture, and downwelling radiation was operated aboard the USNS Bartlett during the first High-Res ARI cruise in September, 1991 by Dr. George Young and graduate student Jeff Hare. The combination of a sonic anemometer for fast response temperature and three-component wind measurements as well as an IR hygrometer for fast response humidity measurements allowed computation of the air/sea fluxes of momentum, heat, and moisture via the inertial dissipation method (Fairall and Larsen, 1986). Jeff Hare has analyzed these observations under the supervision of Dr. Dennis Thomson, and he reported his results at the spring 1992 Hi-Res ARI workshop that was held at APL. These results compare well with measurements from a similar system operated by Dr. Jim Edson of Woods Hole Oceanographic Institute (WHOI) aboard the RV *Oceanus* during the same experiment. However, owing to ship motions, observations of fluxes made on ships may be hard to interpret, as noted in the MS thesis by Hare (1992).

Physical interpretation of these air/sea flux variations across the Gulf Stream front is complicated by mesoscale atmospheric evolution on the same time scale as the ship's transfrontal box patterns. Thus, the meteorological environment often changed significantly in the time required for a ship to complete both its frontal transects and its along-front legs in the two watermasses. The resulting box of air/sea flux observations reflects a mixture of the desired horizontal gradients of air/sea interaction with the unavoidable local temporal change. A primary accomplishment during the first phase of this project has been the development, by Dr. George Young, Todd Sikora, and Jeff Hare,

of a method for using the results of the Penn State atmospheric mesoscale model, which was run in operational mode during the experiment, to interpret these air/sea flux observations. Further studies using this mesoscale model will be performed in phase two of the project.

The signatures of several mesoscale atmospheric and oceanic phenomena are apparent in both the observations and the mesoscale model results. The signatures in the observations would not, however, be interpretable without the vastly superior spatial coverage of the mesoscale model. For example, while the shipboard observations indicate that the large amplitude diurnal cycle of surface stress shown in Figure 1 is primarily a consequence of a diurnal wind cycle, they do not indicate the origin of this wind cycle. Analysis of the mesoscale model results shows that the wind cycle is a phase-lagged response to a diurnal cycle of the horizontal pressure gradient in the High-Res region. This diurnal cycle in the pressure gradient between the Bermuda High and the coastal plain is the result of a diurnally varying pressure trough over the coastal plain in the lee of the Appalachian Mountains. The mesoscale atmospheric model consistently demonstrates the ability to correctly develop and simulate this temporally varying feature even when it is not adequately resolved by the synoptic observations used for model initialization. This success stems from the ability of the model to predict the outcome of the interactions between diurnally varying solar heating and temporally unvarying terrain. The model typically requires about 12 hours to overcome the errors in its initial conditions when there is such predictable diurnal forcing.

The Gulf Stream sea surface temperature front offers another mesoscale forcing feature that is essentially steady on the time scale of the atmospheric mesocirculations. Thus, it is not surprising that the model adequately predicts the associated atmospheric mesocirculations that were observed during the first High-Res cruise. Air/sea flux observations combine with the Penn State mesoscale model forecasts and real-time cloud-field observations from the GOES satellite and the USNS Bartlett to show that the MABL responds vigorously to the sea surface temperature difference across the northwest wall of the Gulf Stream. Significant differences in the surface fluxes across this watermass boundary were observed to result in a sharp change in MABL structure across the boundary. This *atmospheric front* was frequently observed to form in response to the *oceanic front* when benign synoptic conditions brought atmospheric flow along the oceanic front. The resulting atmospheric circulation was reflected by both the enhanced cumulus cloudiness along the front and the convergent wind and stress patterns in the mesoscale model output. Analysis of this mesoscale feedback between ocean and atmosphere is still at a preliminary stage. Use of the mesoscale model to guide interpretation of the above High-Res observations will be pursued by graduate student Sean Sublette in the second phase of the project.

September 16-17, 1991 HI-RES I

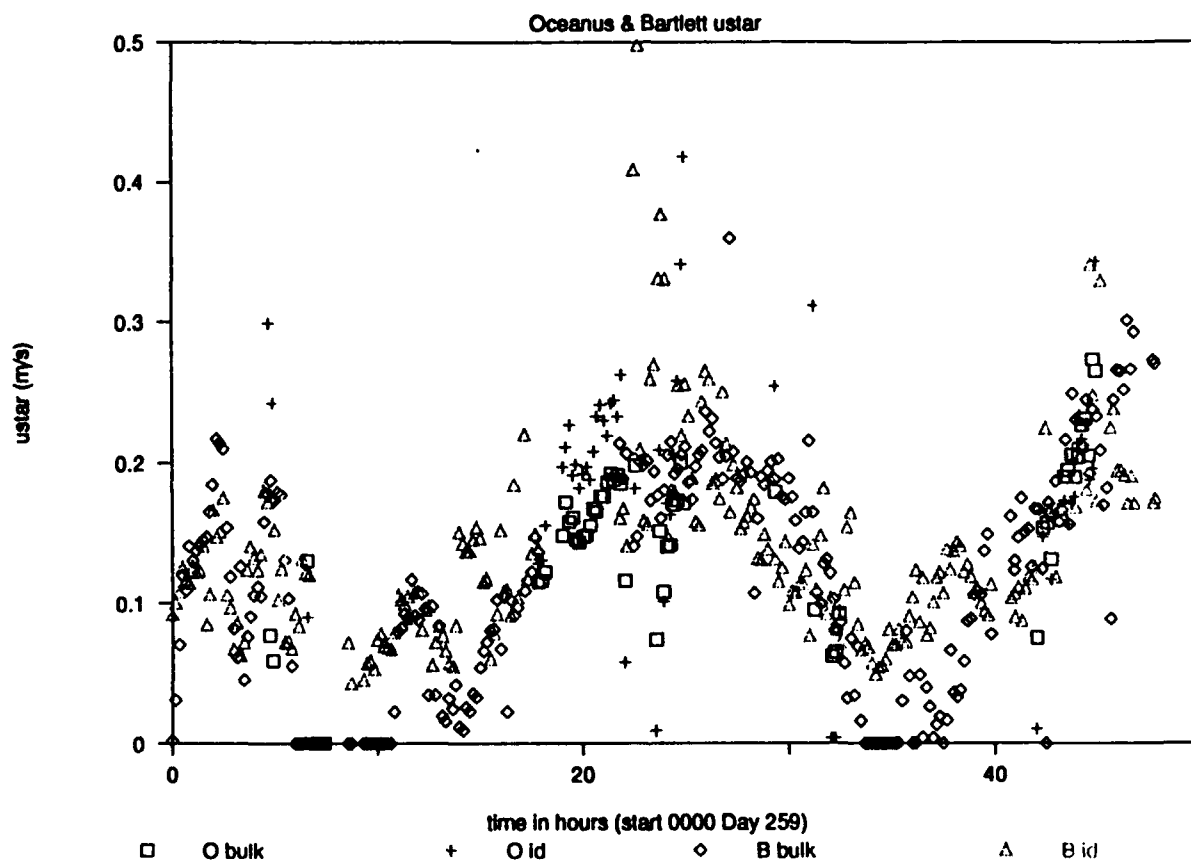


Figure 1. Time series of surface stress u_s calculated using the inertial dissipation (id) and bulk aerodynamic (bulk) methods from observations taken on RV Oceanus (O) and Bartlett (B) during the 48-hour period beginning 00 EDT 16 September 1991.

3. Modeling of submesoscale BL structures

In order to identify the dominant forcing mechanisms and characteristic spatial and temporal responses of the various dynamic and thermodynamic modes of submesoscale MABL convection, we have conducted for a number of years a series of nonlinear modeling studies of BL rolls (Shirer, 1986; Stensrud and Shirer, 1988; Laufersweiler and Shirer, 1989; Haack and Shirer, 1992). An important component of these studies has been comparison of model results with the MABL observations obtained during the KonTur and FIRE [First ISSCP (International Satellite Cloud Climatology Program) Regional Experiment] field programs (Shirer and Brümmer, 1986; Stensrud and Shirer, 1988; Shirer and Haack, 1990). Emphasis has more recently been given to studying the modification of the background wind and temperature profiles by the rolls in order that the probable forcing that produced the rolls could be estimated (Haack and Shirer, 1992; Shirer and Haack, 1990). These nonlinear models also yield profiles of the vertical fluxes of horizontal momentum and heat. These flux profiles are obtained by horizontal integration over one wavelength of the appropriate products given by the model solutions. The spatial and temporal variability of these products gives the spatial and temporal variability of the stress and vertical heat flux through application of either standard bulk aerodynamic or eddy correlation approaches. These approaches are similar to those used in the analysis of observational and Large Eddy Simulation (LES) results (e.g., Businger *et al.*, 1971; Moeng, 1984; Young, 1988).

The above model results have focused on the mid-level properties of the MABL structures, and so it was convenient to assume that the stress and heat flux vanished at the lower boundary. These boundary conditions are clearly not suitable for study of the stress variability at the sea surface, and so during the first two years of our ARI research, Dr. Hampton N. Shirer, Dr. Robert Wells, Julie Schramm, and Peter Bromfield have begun creating new nonlinear, Boussinesq, intermediate-order models of both two- and three-dimensional submesoscale circulations in the MABL. To form the differential equations for these models, we first set the bottom of the domain to be at the top of the surface layer, assumed to be at 10 m above the sea surface, and then we choose lower boundary conditions that are consistent with the wind and temperature profiles typically observed to occur within the surface layer. Dave Ledvina has written a subroutine that uses standard similarity theory (Liu *et al.*, 1979) to give the surface roughness z_0 and Monin-Obukhov length L once the mean wind speed, air/sea temperature difference and humidity difference have been specified. We use the values of z_0 and L from his subroutine to obtain the constants in the boundary conditions via straightforward manipulations of the similarity laws for an unstable environment (e.g., Stull, 1988). Other physical effects represented in the new models include buoyancy, background wind and temperature profiles, Coriolis turning, and height-dependent momentum and temperature dissipation.

To develop the basis functions for the variable expansions used to create the intermediate-order models, we solve eigenfunction problems based on the new boundary conditions; these problems yield nonorthogonal functions for the vertical structure of the variables that are expressible using exponential and trigonometric functions. These

functions, as well as the differential equations for the models, are obtained symbolically with the aid of the programs Derive and MAPLE. The results are output by Derive and MAPLE in FORTRAN format for convenient insertion into the numerical codes for simulation of the MABL circulations. Significantly, this approach allows relatively straightforward extensions of the models. The FORTRAN code is in the final stages of debugging; preliminary results indicate that the stress and heat flux profiles have the same qualitative form as that seen, for example, in the submesoscale MABL observations in Figure 9 of Brümmer and Busack (1990).

However, because some of the boundary conditions act as a sink of energy while others act as a source, care must be taken in the way that the perturbation pressure is handled in the three-dimensional model. A reformulation of the first version of the model created by Julie Schramm is an early task of phase two of the study. This reformulation, which will be undertaken by graduate student Louis Zuccarello, will use the vector vorticity equation as a device for circumventing the need to explicitly represent the pressure perturbation. In addition, a separate two-dimensional model based on the along-roll component of the vorticity is being created by graduate student Peter Bromfield.

The versions of the intermediate-order models currently being developed represent two- and three-dimensional structures that have a single horizontal wavelength. As a consequence, the results from these versions of the model will provide estimates of only the symmetric component of sea surface stress variability. However, for the comparison with observations using conditional sampling of updrafts and downdrafts in the lower portion of the domain, we will need to include at least three horizontal wavenumbers in the variable expansions for the model. In this extended model to be developed in phase two of the project, we expect to maintain the same level of resolution in the vertical, and so this extension will be relatively straightforward to complete with the aid of Derive or MAPLE. This new level of resolution will be compatible with the aircraft data analysis by Todd Sikora, who gives the surface layer patterns of the vertical fluxes of heat and momentum in updrafts and downdrafts (section 4 and Appendix A). In our comparison with these observations, we will determine in particular whether the modeled stress patterns agree with the observed ones that are only weakly dependent on the degree of instability, or thermal forcing.

Once fully extended, the above models will be ready for study of both idealized profiles and the ones observed during the KonTur, FIRE, ASTEX and High-Res MABL field programs. To compare our results with High-Res cases, we must supplement the wind and temperature profiles measured using ship-based sensors with profiles derived from the Penn State mesoscale model forecasts, owing to difficulty in interpreting the ship-based measurements of these profiles (section 2).

Because the initially developing solutions of the intermediate-order model are temporally periodic (which corresponds to downwind propagation of the convective circulations), we can obtain the expected wavelength and orientation of the MABL structures. These wavelengths and orientations can be compared with those inferred from

available ERS-1 SAR images or visible satellite imagery. The resulting solutions can be conditionally sampled in a way similar to that used by Todd Sikora, who, during the first phase of the study, has documented the coarse horizontal variability of the stress patterns in updrafts and downdrafts measured at 50 m above the sea surface during FIRE; these results are summarized in the next section and Appendix A. In addition, similar conditional sampling strategies will be used to compare the model solutions with the sodar-derived structures of the vertical velocity within thermals that were measured during the first High-Res cruise and that are expected to be measured during the main cruise in 1993.

4 Analysis of BL observations

As noted earlier, mesoscale circulations and submesoscale MABL convective structures are being emphasized in our observational analyses during phases one and two of our work because they are the primary atmospheric modulators of surface stress on the mesoscale and submesoscale spatial and temporal scales in the High-Res region of the Gulf Stream. The primary goal of our analyses is the development of quantitative conceptual models of these mesoscale and submesoscale circulations within different large-scale atmospheric regimes. The major objective is the determination of the temporal and spatial patterns of mesoscale and submesoscale surface stress and heat flux variability for each observed case, stratified where possible by appropriate large-scale forcing as measured by the controlling parameters.

The quantitative observational description of the role of submesoscale MABL convection in causing horizontal air/sea flux variability was summarized in the MS thesis by Sikora (1992), was presented at the Tenth Symposium on Turbulence and Diffusion (Sikora and Young, 1992) and will appear in *Boundary Layer Meteorology* (Sikora and Young, 1993, which is Appendix A). Aircraft turbulence measurements made during the first stratocumulus phase of FIRE (Albrecht *et al.*, 1988) that was conducted under the 1986-1991 ONR-funded University Research Initiative (URI) at Penn State provided the primary data source. Todd Sikora in his MS research (Sikora, 1992) prepared horizontal planviews depicting the typical surface layer patterns of the vertical fluxes of momentum, heat, and moisture associated with the updraft and downdraft components of submesoscale convective structures in the MABL. For example, Figure 2 shows the corresponding composite planview perturbation wind field for MABL convective downdrafts, the phenomenon that causes "cat's paw" wave patterns at the sea surface. Physical interpretation of these flux patterns shows that these flux patterns exhibit only limited sensitivity to large-scale atmospheric and oceanic conditions. While the patterns can differ significantly between stable and unstable atmospheric boundary layers, they are essentially similar over a broad range of unstable conditions. Thus, these submesoscale flux patterns are expected to be rather ubiquitous within the MABL. These results can be used by ocean-wave modelers to quantify the horizontal variability of atmospheric forcing on spatial scales on the order of 0.1 to 1.0 km.

Planview of Composite Downdraft Horizontal Wind

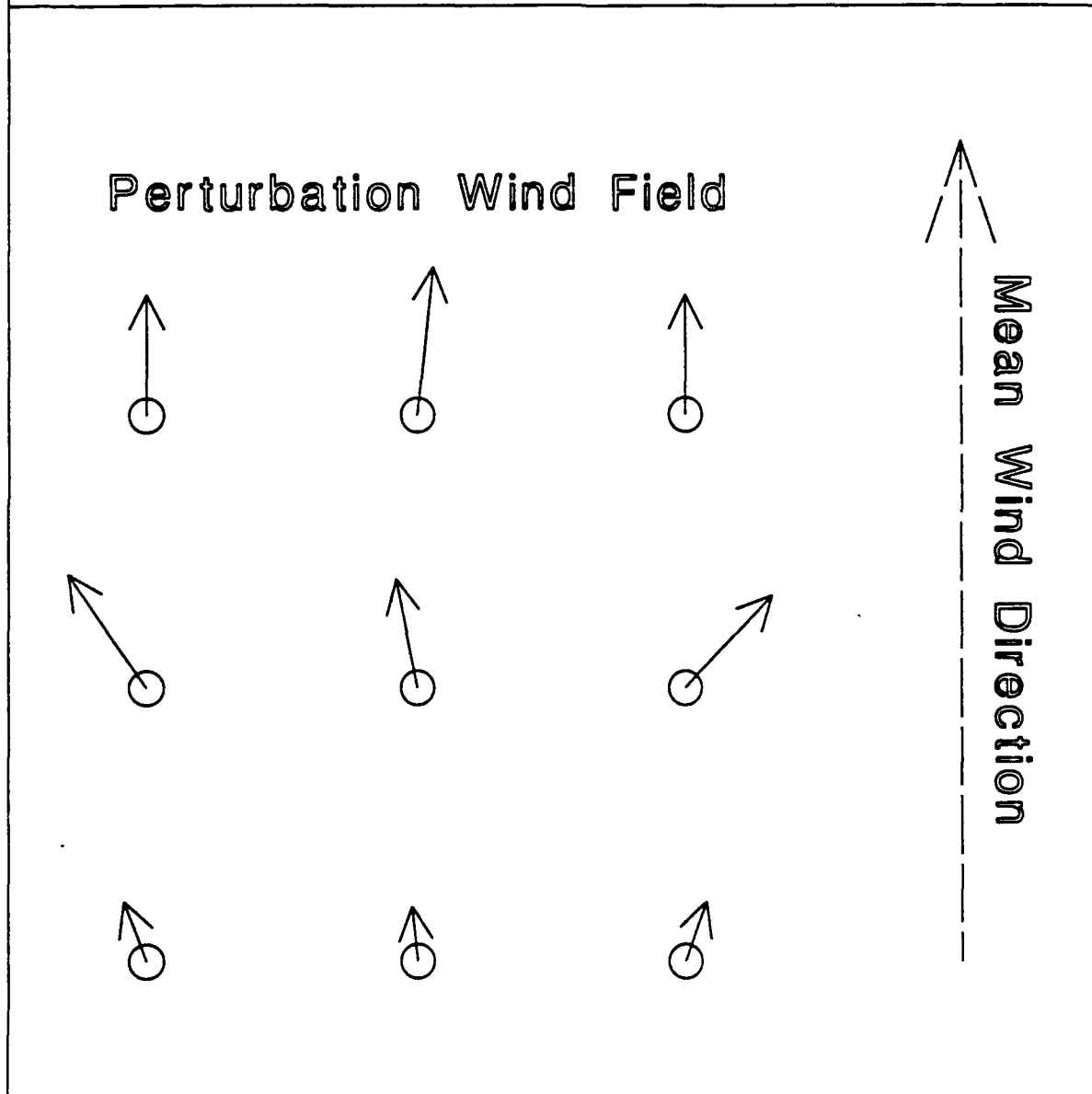


Figure 2. Planview of composite horizontal wind the MABL convective downdrafts in the surface layer (after Sikora and Young, 1993).

As the observational study of MABL convection is complete, the only task remaining in this aspect of the project is to use these results in the modeling effort described above in section 3. During the second phase of this work, these results will be used to guide the final stages of model development as well as for the verification and interpretation of model results. Of particular interest is whether the model corroborates the observed relatively weak dependence of the flux patterns on the degree of instability.

5. An improved correlation dimension algorithm

The atmospheric structures responsible for creating stress variability at the sea surface are clearly chaotic, and there remains a major challenge for scientists to suitably quantify this chaotic structure. Existing algorithms for estimating the correlation dimension d typically produce results that are difficult to interpret and that are subject to errors whose magnitudes are not typically estimated. We have developed a new objective algorithm (Wells *et al.*, 1993 and Appendix B) that overcomes these difficulties because it is based on hypotheses that are more likely to be satisfied than are the ones for the standard approach. Not only does this method in principle produce an infinite number of estimates for the correlation dimension, but it also gives error estimates that, when minimized, produce the optimal value for d . This algorithm is developed and tested in a manuscript that has been submitted to *Physica D* (Wells *et al.*, 1993 and Appendix B); a preliminary version was presented as a poster at the Spring 1992 AGU meeting in Montreal (Wells *et al.*, 1992). Christian Fosmire in his MS thesis work (Fosmire, 1993) tests this algorithm using time series data from both the standard Lorenz and Henon attractors and from sodar data measured in a 1988 field experiment conducted near Penn State. In addition, in collaboration with Dr. Dennis Thomson, Dr. Harry Henderson has been applying this and other algorithms to BL measurements (e.g., Thomson and Henderson, 1991, 1992; Thomson *et al.*, 1991).

References

- Albrecht, B.A., D.A. Randall, and S. Nicholls, 1988: Observations of marine stratocumulus during FIRE. *Bull. Am. Meteor. Soc.*, **69**, 618-626.
- Alpers, W.R., D.B. Ross, and C.L. Rufenbach, 1981: On the detectability of ocean surface waves by real and synthetic aperture radar. *J. Geophys. Res.*, **86**, 6481-6498.
- Brümmer, B. and B. Busack, 1990: Convective patterns within a field of stratocumulus. *Mon. Wea. Rev.*, **118**, 801-817.
- Businger, J.A., J.C. Wyngaard, Y. Izumi, and E.F. Bradley, 1971: Flux profile relationships in the atmospheric surface layer. *J. Atmos. Sci.*, **28**, 181-189.
- Fairall, C.W. and S.E. Larsen, 1986: Inertial-dissipation methods and turbulent fluxes at the air-ocean interface. *Boundary-Layer Meteorology*, **34**, 287-301.
- Fosmire, C.J., 1993: Estimating the correlation dimension of observed boundary layer winds. MS Thesis, Penn State University, in preparation.
- Gerling, T.W., 1985: Remote sensing of the ocean-surface wind field with a scatterometer and a synthetic aperture radar. *John Hopkins APL Digest*, **6**, 320-329.
- Gerling, T.W., 1986: Structure of the surface wind field from the Seasat SAR. *J. Geophys. Res.*, **91**, 2308-2320.
- Haack, T. and H.N. Shirer, 1992: Mixed convective/dynamic roll vortices and their effects on initial wind and temperature profiles. *J. Atmos. Sci.*, **49**, 1181-1201.
- Hare, J.E., 1992: Shipboard eddy-covariance measurements of the turbulent fluxes of heat, moisture, and momentum. MS Thesis, Penn State University, 207 pp.
- Laufersweiler, M.J. and H.N. Shirer, 1989: A simple dynamical model of a stratocumulus-topped boundary layer. *J. Atmos. Sci.*, **46**, 1133-1153.
- Liu, W.T., K.B. Katsaros, and J.A. Businger, 1979: Bulk parameterization of the air-sea exchanges of heat and water vapor including the molecular constraints at the interface. *J. Atmos. Sci.*, **36**, 1722-1735.
- Moeng, C.-H., 1984: A large-eddy-simulation model for the study of planetary boundary layer turbulence. *J. Atmos. Sci.*, **41**, 2052-2062.
- NASA, 1988: SAR synthetic aperture radar instrument panel report. *Earth Observing System Reports*, **III**, 233 pp.

- Phillips, O.M., 1988: Remote sensing of the sea surface. *Ann. Res. Fluid Mech.*, **20**, 89-109.
- Shirer, H.N., 1986: On cloud street development in three dimensions: Parallel and Rayleigh instabilities. *Contrib. Atmos. Phys.*, **59**, 126-149.
- Shirer, H.N. and B. Brümmer, 1986: Cloud streets during KonTur: A comparison of parallel/thermal modes with observations. *Contrib. Atmos. Phys.*, **59**, 150-161.
- Shirer, H.N. and T. Haack, 1990: The modification of large-scale wind profiles by roll circulations. *Proc. Seventh Conf. on Atmos. Rad.*, San Francisco, CA, Amer. Meteor. Soc., J113-J118.
- Sikora, T.D., 1992: Air/sea flux patterns within convective structures of the marine atmospheric surface layer, MS Thesis, Penn State University, 28 pp.
- Sikora, T.D. and G.S. Young, 1992: Air/sea flux patterns within convective structures of the marine atmospheric surface layer, Preprints, *Tenth Symposium on Turbulence and Diffusion*, Sept. 29-Oct. 2, 1992, Portland, OR, American Meteorological Society, 25-27.
- Sikora, T.D. and G.S. Young, 1993: Observations of planview flux patterns within convective structures of the marine atmospheric surface layer, *Boundary Layer Meteorology*, **35**, in press.
- Stensrud, D.J. and H.N. Shirer, 1988: Development of boundary layer rolls from dynamic instabilities. *J. Atmos. Sci.*, **45**, 1007-1019.
- Stull, R.B., 1988: *An Introduction to Boundary Layer Meteorology*. Kluwer Academic Publishers, Boston, 666 pp.
- Thomson D.W. and H.W. Henderson, 1991: Attractor-based interpretation of measurements made with radar and acoustic remote sensing systems. *EPP-Fall 1991 Symposium on Remote Sensing of the Propagation Environment*, Sept. 30-Oct. 4, 1991, Cesme-Ismir, Turkey.
- Thomson, D.W. and H.W. Henderson, 1992: Definition of local atmospheric attractors using measurements made with surface-based remote sensing systems. *Proc. of the First Experimental Chaos Conference*, Oct. 1-3, 1991, Arlington, VA. World Scientific Publishing Co., 389-402.
- Thomson, D.W., H.W. Henderson, and C.J Fosmire, 1991: Using remote sensing systems to estimate attractors for meteorological variables. Preprints, *Second Symposium on Tropospheric Profiling: Needs and Technologies*, Boulder, CO, Sept. 10-13, 1991.

- Visecky, J.F. and R.H. Stewart, 1982: The observation of ocean surface phenomena using imagery from the SEASAT synthetic aperture radar: An assessment. *J. Geophys. Res.*, **87**, 3397-3430.
- Wells, R., H.N. Shirer and C.J. Foscire, 1992: An improved algorithm for calculating the correlation dimension and for estimating its probable error, AGU Spring 1992 Conference, May 12-16, 1992, Montreal, Canada, American Geophysical Union.
- Wells, R., H.N. Shirer, C.J. Foscire and J.A. Doran, 1993: Improved algorithms for estimating the correlation dimension and the associated probable errors. Submitted to *Physica D*.
- Young, G.S., 1988: Turbulence structure of the convective boundary layer. Part I: Variability of normalized turbulence statistics. *J. Atmos. Sci.*, **45**, 719-726.

PUBLICATIONS/PRESENTATIONS/REPORTS
SAR-RELATED STRESS VARIABILITY IN THE
MARINE ATMOSPHERIC BOUNDARY LAYER (MABL)

Journal Articles:

Sikora, T.D. and G.S. Young. Observations of planview flux patterns within convective structures of the marine atmospheric surface layer, *Boundary Layer Meteorology*, **35**, in press (1993).

Wells, R., H.N. Shirer, C.J. Foscire and J.A. Doran. Improved algorithms for estimating the correlation dimension and the associated probable errors. Submitted to *Physica D*. (1993)

Conference Papers:

Sikora, T.D and G.S. Young. Air/sea flux patterns within convective structures of the marine atmospheric surface layer, Preprints, *Tenth Symposium on Turbulence and Diffusion*, Sept. 29-Oct. 2, 1992, Portland, OR, American Meteorological Society, 25-27 (1992).

Thomson, D.W., H.W. Henderson, and C.J Foscire. Using remote sensing systems to estimate attractors for meteorological variables. Preprints, *Second Symposium on Tropospheric Profiling: Needs and Technologies*, Boulder, CO, Sept. 10-13, 1991 (1991).

Thomson, D.W. and H.W. Henderson. Attractor-based interpretation of measurements made with radar and acoustic remote sensing systems. *EPP-Fall 1991 Symposium on Remote Sensing of the Propagation Environment*, Sept. 30-Oct. 4, 1991, Cesme-Ismir, Turkey (1991).

Thomson, D.W. and H.W. Henderson. Definition of local atmospheric attractors using measurements made with surface-based remote sensing systems. *Proc. of the First Experimental Chaos Conference*, Oct. 1-3, 1991, Arlington, VA. World Scientific Publishing Co., 389-402 (1992).

Wells, R., H.N. Shirer and C.J. Foscire. An improved algorithm for calculating the correlation dimension and for estimating its probable error, AGU Spring 1992 Conference, May 12-16, 1992, Montreal, Canada, American Geophysical Union (1992).

Theses:

Fosmire, C.J. Estimating the correlation dimension of observed boundary layer winds. MS Thesis, Penn State University, in preparation (1993).

Hare, J.E. Shipboard eddy-covariance measurements of the turbulent fluxes of heat, moisture, and momentum. MS Thesis, Penn State University, 207 pp. (1992).

Sikora, T.D. Air/sea flux patterns within convective structures of the marine atmospheric surface layer, MS Thesis, Penn State University, 28 pp. (1992).

PERSONNEL FUNDED IN PART BY
SAR-RELATED STRESS VARIABILITY IN THE
MARINE ATMOSPHERIC BOUNDARY LAYER (MABL)

Faculty: Dr. Hampton N. Shirer and George S. Young

Postdoctoral associate: Dr. Harry W. Henderson

Research Associates: Dave Ledvina, Julie Schramm

Graduate Students: Peter Bromfield, Christian Fosmire, Jeff Hare, Julie Schramm, Todd
Sikora

APPENDIX A

OBSERVATIONS OF PLANVIEW FLUX PATTERNS WITHIN CONVECTIVE
STRUCTURES OF THE MARINE ATMOSPHERIC SURFACE LAYER

Todd D. Sikora and George S. Young

The Pennsylvania State University

November 1992

1. Introduction

The marine atmospheric surface layer (MASL) ($Z \leq 0.1 Z_i$ where Z_i is the boundary layer depth) (Stull, 1989) plays a major role in air/sea interaction. It is the MASL that couples the sea surface to the overlying atmospheric boundary layer through vertical eddy fluxes (hereafter referred to simply as fluxes), such as those of buoyancy, moisture, and momentum. While these fluxes are present in both stable and unstable environments, they tend to be enhanced by convective elements, as is implied by bulk aerodynamic parameterization (e.g. Liu et al., 1979). For this reason, much of the recent research in this area has concentrated on the convective marine atmospheric surface layer (CMASL).

CMASL fluxes are realized through sub-mesoscale convective updrafts (CUs) and downdrafts (CDs). These features have diameters on the order of tens to thousands of meters (Lenschow and Stephens, 1980). Khalsa and Greenhut (1985) found that within a central Pacific CMASL, such features were responsible for 75% of the total flux of heat, moisture, and momentum. This importance provides the motivation to explore further the flux characteristics of CMASL drafts.

Various methods may be employed to study CMASL drafts. Qualitatively, this can be accomplished by simply observing the effects their associated fluxes have on the environment. On a human scale, anyone who has enjoyed a day of sailing,

seen wisps of sea fog, or witnessed cats paws rippling across a body of water has personally sensed the impact of CMASL drafts on the environment. Another example of this manifestation can be seen in Figures 1 and 2 of Sikora and Young (submitted to *Boundary Layer Meteorology*, November 1992). Figure 1 is a visible image from the Kosmos 1500 (Okean) satellite. The image is centered at 26° N 125.5° W and is dated July 11, 1984. It shows common boundary layer cumuliform clouds, horizontal scales of which are on order of the boundary layer depth, induced by fluxes of heat and moisture within CMASL-born CUs. Figure 2 is the corresponding X-band real aperture radar image of the underlying sea surface. It depicts a perturbed sea surface wave pattern resulting from CMASL momentum flux patterns driven by flow into CUs and out of CDs.

In order to obtain data on the effects and structure of CUs and CDs in a more quantitative sense, various techniques have been employed, including observations from a sensor equipped catamaran (Dorman and Mollo-Christensen, 1973), the use of acoustic sounders (Gaynor and Mandics, 1978), and observations of sea gulls in flight (Woodcock, 1940, 1975). Data for the quantitative study in this paper are obtained from NCAR Electra aircraft flights during the First ISCCP (International Satellite Cloud Climatology Project) Regional Experiment (FIRE). Flights were conducted over a several hundred kilometer region west of the southern California coast during June and July, 1987. For detailed reviews of the FIRE

project, see Albrecht et al. (1988) and Kloesel et al. (1988).

The traditional way to investigate the flux characteristics of boundary layer features is through conditional sampling and composite analysis, examples of which are discussed below. Simply put, conditional sampling uses an indicator function to isolate from a dataset features of interest (e.g. CUs and CDs). Composite analysis then combines information from these selected features to determine their average spatial structure.

In the past, various studies have gathered valuable information concerning boundary layer features using these sampling and analysis techniques. Wilczak and Tillman (1980) and Wilczak (1984) used Boulder Atmospheric Observatory tower data to produce detailed, land-based, statistics for convective atmospheric surface layer features known as temperature ramps. Young (1988) also investigated land-based turbulence at the Boulder Atmospheric Observatory. He conditionally sampled aircraft data, based upon vertical velocity perturbations and mixed layer spectra of vertical velocity and temperature, in order to analyze thermals within the convective boundary layer. Lenschow and Stephens (1980) used NCAk Electra aircraft data to generate information on the structure of marine atmospheric boundary layer (MABL) thermals using humidity as an indicator function. Greenhut and Khalsa (1982) and Khalsa and Greenhut (1985) also used aircraft data to study properties of drafts in the MABL but, as in Young (1988), they used vertical velocity as an indicator of a

feature. In addition to observational studies, large-eddy simulation models, such as that of Schumann and Moeng (1991), have been used to provide boundary layer datasets for conditional sampling and compositing.

While previous work has resulted in detailed vertical profiles of properties of MABL updrafts and downdrafts, information on planview flux variability of CMASL CUs and CDs is lacking. To fill this need, this study utilizes conditionally sampled and composited eddy correlated FIRE aircraft data to investigate the typical CMASL CU and CD planview patterns of vertical velocity flux, $\overline{w'w'}$, buoyancy flux, $\overline{w'T_v'}$, absolute humidity flux, $\overline{w'r'}$, and along-mean-wind momentum flux, $\overline{w'u'}$. Note that while CUs and CDs are segregated in this study, the techniques used for their analyses are identical.

2. Procedures

The use of NCAR Electra turbulence data from project FIRE is advantageous for the type of research discussed here because a properly instrumented aircraft provides a means for collecting high resolution turbulence data from a large number of CMASL drafts. While each draft can be penetrated only once, penetrations of many different drafts can be made from numerous angles. In addition, the turbulence data from a draft sampled by an aircraft can be looked upon as a snapshot of that feature (see sub-section 2.3.). The result, after data processing, conditional sampling, and compositing, is a statistically robust planview flux description of a typical CMASL draft.

2.1. FLIGHT INFORMATION

Of the numerous available datasets collected from Electra flight legs during FIRE, only the 20 used in this study were conducted within the CMASL. These legs averaged 50 km (500 sec) in length (duration). These legs were flown on seven different days, during which the average boundary layer depth was 920 m. The legs were flown at a height of 50 m, well within the depth of the surface layer. The ratio of the boundary layer depths to the Monin-Obukhov lengths ranged from -0.62 to -37.56, indicative of slightly to moderately unstable MABLs. While flux intensity differences for CUs and CDs are

seen within this stability range, the "flux-shapes" (the patterns of spatial variation of flux magnitude across a draft) are similar. This pattern similarity in the presence of intensity differences is exactly analogous the geometric similarity of "similar triangles" of varying sizes. Structural differences are, however, observed for stable and extremely unstable cases. Insufficient data prevented the extension of the composite analysis to these other stability ranges.

2.2. INSTRUMENTATION AND DATA PROCESSING

The Electra CMASL 20 hz turbulence data used in the present study include vertical velocity, w , air temperature, T , absolute humidity, r , and the aircraft-oriented components of the wind, u , and, v . This sampling rate combined with the 100 m/s aircraft speed yields a minimum resolvable wavelength of 10 m. A review of the aircraft instrumentation of significance to this study can be found in Nucciarone and Young (1991). Data processing for mean, trend, and spike removal, as well the derivation of buoyancy flux, parallels that of Moyer and Young (1991). In order to eliminate contributions by mesoscale phenomena in the data, high-pass filtering is employed following the techniques of Young (1987,1988).

An example of the spectral response of the filter can be seen in Figure 1. The figure shows, for a cosine wave, how

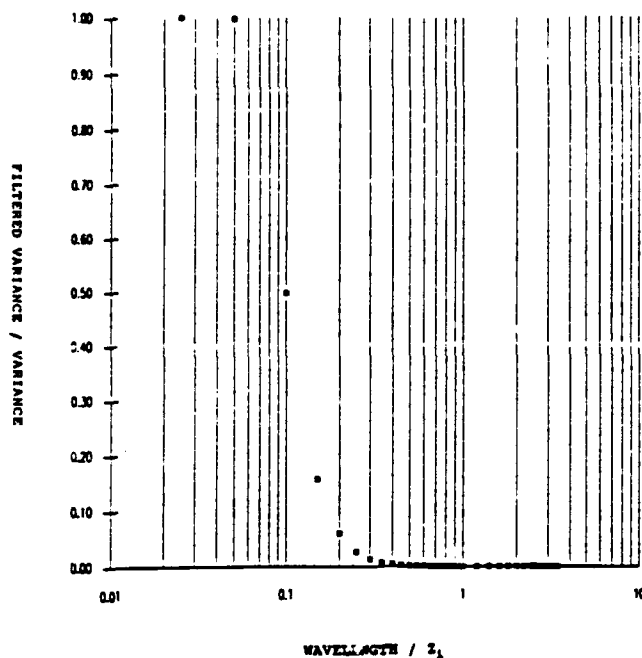


Fig. 1. An example of the spectral response of the filter.

the ratio of the wave's filtered variance to its unfiltered variance varies with the ratio of wavelength to Z_i . In this example, the cutoff wavelength chosen is $0.1 Z_i$. At this wavelength, 50% of the wave's original variance remains. At longer wavelengths, the amount of the wave's original variance remaining after filtering diminishes rapidly.

FIRE spectra of Nucciarone and Young (1991) indicate that $1.5 Z_i$ is the appropriate mesoscale subrange cutoff wavelength for use in the filter. The net result of this data processing, for any one variable, is a sub-mesoscale perturbation series (denoted by primed variables) suitable for computing eddy correlation statistics.

Coordinate rotations are performed on the perturbation wind components yielding one component in the direction of the

mean wind, u' , and another aligned with positive values 90° to the left of the mean wind, v' . Unlike that seen in Geernaert and Hansan (1992), where orographic distortion of the low level flow may be occurring, the cross-mean-wind components of the momentum fluxes of this study are both statistically and physically insignificant when compared with the along-mean-wind component (i.e. mean $<$ standard deviation for $\overline{w'v'}$ and $\overline{w'v'} \ll \overline{w'u'}$). For this reason, the cross-mean-wind momentum flux will not be discussed.

2.3. CONDITIONAL SAMPLING

In order to distinguish updrafts and downdrafts, event criteria based on perturbation vertical velocity are required. Greenhut and Khalsa (1982) and Young (1988) show that w' event criteria, incorporating germane horizontal scales and magnitude thresholds, allow for the proper detection of boundary layer features of interest.

In order to distinguish CUs and CDs, the w' series is first band-pass filtered to retain only the convective scales (Young 1988). The band-pass filter is a variation on that discussed in sub-section 2.2., combining both a high-pass and low-pass stage. It is designed to eliminate both the mesoscale and inertial subrange contributions to the w' series, while still preserving the CUs and CDs of the energy containing subrange. As discussed in sub-section 2.2., $1.5 Z_i$ is used as the mesoscale subrange cutoff wavelength. The

choice of an inertial subrange cutoff wavelength is $0.1 Z_i$. As in Young (1988), this choice eliminates scales of motion associated with the inertial cascade.

Given the average Z_i of this study, a minimum draft width of 50 m is chosen so that the narrowest acceptable event (CU/CD couplet) corresponds with the $0.1 Z_i$ inertial subrange cutoff wavelength used in the band-pass filter. All drafts not meeting the minimum width criteria are rejected because of their inertial subrange character.

The literature mentioned in section 1. provides numerous examples of conditional sampling magnitude thresholds designed to distinguish features of interest from their environment. Inspection of the FIRE w' data series suggests that a w' threshold of ± 0.1 m/s eliminates disorganized areas of weak ascent or descent. Any data points for which $w' < 0.1$ m/s are therefore considered not to be part of significant convective features and are so rejected.

CUs (CDs) are then defined to be features within the band-pass filtered w' data series meeting these minimum width and magnitude criteria. The total number of CUs sampled and used in compositing is 2839, averaging 98 m in width and occupying 28% of the data series. The total number of CDs sampled and used in compositing is 3062, averaging 107 m in width and occupying 33% of the data series. Given the above widths and an aircraft velocity of 100 m/s, it can be shown that Taylor's Hypothesis is valid (Stull 1989). Draft composites of eddy correlation statistics can therefore be

looked upon as typical planview flux snapshots of a CU or a CD.

2.4. COMPOSITING OF EDDY CORRELATION STATISTICS

After the isolation of CUs and CDs, eddy correlation fluxes of vertical velocity, buoyancy, absolute humidity, and along-mean-wind momentum are calculated from the high-pass filtered dataset, for each draft. Note that, unlike the band-passed series used to locate the sub-mesoscale CUs and CDs, this series retains the inertial subrange contributions. Only the mesoscale contributions are filtered out, as discussed in sub-section 2.2.. In order to develop typical planview flux snapshots, the fluxes from all the drafts are composited together using the series of averaging calculations and grouping techniques discussed below.

Each draft is first divided into 3 bins of equal length: the aircraft entry region of the draft, bin (a), the middle of the draft, bin (b), and the aircraft exit region of the draft, bin (c). The average CU and CD flux patterns for each leg are then found by calculating bin average eddy correlation statistics as follows. The flux of any variable y by variable w' is found by first taking the sum of their product over all points of all like bins [bin (a), (b), or (c)] over all like drafts (CUs or CDs) within the leg. This sum is then divided by the number of data points in all like bins of all like drafts within the leg.

The resulting 40 leg average drafts (LADs) from the 20 flight legs are then separated into one of 3 equal angular-width groups. The grouping of an LAD depends on the path taken by the aircraft, through the draft, relative to the mean wind. In polar coordinates with the mean wind vector aligned towards 0° , these relative heading groups are: along-mean-wind (330° to 30° and 150° to 210°), cross-mean-wind (60° to 120° and 240° to 300°), and diagonal-to-the-mean-wind (the remaining relative heading ranges).

To maintain wind-relative consistency in bin naming, flux data for bins (a) and (c) are switched for those drafts of the along-mean-wind and diagonal groups whose relative headings oppose the mean wind. The same is done for LADs of the cross-mean-wind group whose relative heading range is aligned to the left of the mean wind. Note that while there are twice as many relative heading ranges for the diagonal group as for the other two, the angular width of each heading range in the diagonal group is only half as large as for the other two. Thus, the angular coverage of all 3 groups is equal.

The two remaining relative-heading ranges of the diagonal group (30° to 60° and 300° to 330°) can be merged using symmetry arguments. Wilczak (1984) shows mirror symmetry of the horizontal perturbation wind field about an axis aligned with the mean wind extending through the center of his large-scale eddy (LSE which is a CU/CD couplet). A similar symmetry can be seen in the current dataset by examination of the fluxes of the cross-mean-wind group composites found in

section 3.. Comparison of the data from the two relative heading ranges of the diagonal group (not shown) demonstrates symmetry across the axis of the mean wind for both the upwind and downwind ends of the drafts. Taking these symmetries into account, flux data of like LAD downwind bins of the diagonal group are composited together as are flux data of upwind bins. Figure 2 shows the spatial relation of the three groups within a planview draft. Bins are labeled (a), (b), or (c). Upper case letters indicate the group to which each bin belongs; the along-mean-wind group (A), the cross-mean-wind group (C), and the diagonal-to-the-mean-wind group (D). The mean wind vector is assumed to be directed towards the top of the figure.

The process of compositing flux data of like LAD bins into a flux for the corresponding bins of a group average draft (GAD) will now be explained. First, because the center bin for all groups corresponds to the same part of the draft, the average bin (b) flux over all like LADs over all groups (bin (b) average) may be used to represent the flux in the center bin of all groups. As stated in sub-section 2.1., drafts of each leg are structurally similar in terms of their flux-shape. However, there is a need to correct for mean draft intensity differences between like bins of different LADs. It follows then that LAD bin (a) and (c) fluxes are rescaled before any averaging to produce GADs. This rescaling uses a correction coefficient based on the need for inter-leg similarity in bin (b), described above. This correction

coefficient is bin (b) average divided by the respective LAD bin (b). This approach is robust because the LAD bin (b) fluxes of all the quantities studied are generally large and of same sign.

The final planview composite is found by simply overlaying the along-mean-wind, cross-mean-wind, and diagonal-to-the-mean wind (again using symmetry for the second diagonal) GADs for each statistic discussed.

cD	cA	cD
aC	bACD	cC
aD	aA	aD

Fig. 2. The spatial relation of the three groups within a planview draft.

3. Observational Results

Planview draft flux composites of vertical velocity, buoyancy, absolute humidity, and the along-mean-wind component of momentum, along with corresponding bin standard deviations, are presented in Tables I through VIII. Each table is a three by three array of group bin fluxes. Bin location in this array corresponds to its position within the composite draft. In all tables, the mean wind is directed towards the top of the table. For each composite, then, the along-mean-wind group axis is aligned from the upwind center to downwind center, the cross-mean-wind group axis is aligned from the middle left to middle right, and the diagonal group makes up the remainder.

Note that the middle center bin of all tables is its respective bin (b) average of sub-section 2.4.. Recall also that the middle center bin is used to rescale all other bins within a flux composite. For these reasons, the majority of the uncertainty associated with any flux-shape and intensity related interleg differences, associated with interleg differences in the middle center bins, is forced into the perimeter of the composite array. It follows then that standard deviations for the middle center bins are not given.

3.1. VERTICAL VELOCITY FLUX

Vertical velocity dictates, to a large extent, the other

flux patterns discussed in this study. Not only is it used for the defining of events, but also it is the flux variable doing the work, so to speak, by advecting the other quantities. The planview CU $\overline{w'w'}$ composite is presented in Table I.

TABLE I

CU vertical velocity flux composite and corresponding standard deviations.

$\overline{w'w'} (m^2s^{-2})$ (std. dev.)	Left	Center	Right
Downwind	0.227 (0.015)	0.244 (0.040)	0.227 (0.015)
Middle	0.217 (0.023)	0.341	0.225 (0.021)
Upwind	0.238 (0.009)	0.266 (0.016)	0.238 (0.009)

Because all bin standard deviations are much smaller than the bin fluxes, there is statistical confidence in the entire CU $\overline{w'w'}$ composite. The strongest flux region is found along the along-mean-wind group axis with the largest magnitude of flux being at the center of the composite. This shape compares well with that found at 50 m over land by Wilczak

(1984). Examining the perimeter of the composite, the flux magnitude along the upwind side of the draft tends to be larger than that along the downwind side, although these asymmetries are less statistically significant than the radial variation. The weakest flux is found in the middle right and left bins.

The planview CD vertical velocity flux composite is shown in Table II. As with the CU composite, there is

TABLE II

CD vertical velocity flux composite and corresponding standard deviations.

$\overline{w'w'} (m^2s^{-2})$ (std. dev.)	Left	Center	Right
Downwind	0.160 (0.011)	0.161 (0.018)	0.160 (0.011)
Middle	0.171 (0.024)	0.204	0.173 (0.024)
Upwind	0.162 (0.009)	0.166 (0.019)	0.162 (0.009)

statistical confidence in all bin fluxes. While the largest magnitude of $\overline{w'w'}$ is again found in the center middle bin, the over all flux composite is weaker than that of the CU. This

finding is in agreement with those of Greenhut and Khalsa (1982) for their coherent downdrafts. As with the CU composite, other aspects of the $\overline{w'w'}$ pattern are less statistically significant. The strongest flux region is found along the cross-mean-wind group axis. Flux along the upwind side of the draft is slightly larger than that along the downwind side.

3.2. BUOYANCY FLUX

The buoyancy flux of the current study has the same sign and approximates to a large extent the magnitude of the heat-flux $\overline{w'T'}$. The planview CU buoyancy flux composite is presented in Table III. While the composite corners lack statistical significance, there is statistical confidence in that part of the composite consisting of the along-mean-wind and cross-mean-wind groups. Along these axes, general symmetries exist with strongest $\overline{w'T'_v}$ being at the middle center of the composite. All fluxes within the composite are down-gradient. This finding is in agreement with those of Khalsa and Greenhut (1985) for their lowest levels.

The planview CD buoyancy flux composite is presented in Table IV. Statistical significance in the $\overline{w'T'_v}$ pattern is similar to that of the CU. The along-mean-wind and cross-mean-wind group axes are more symmetric than in the CU while the diagonal-to-the-mean-wind group axis is even more

TABLE III

CU buoyancy flux composite and corresponding standard deviations.

$\overline{w'T_v'}$ (ms ⁻¹ °C) (std. dev.)	Left	Center	Right
Downwind	0.024 (0.021)	0.010 (0.002)	0.024 (0.021)
Middle	0.010 (0.002)	0.018	0.011 (0.002)
Upwind	0.006 (0.008)	0.014 (0.002)	0.006 (0.008)

asymmetric in the along-mean-wind direction than in the CU.

The pattern of the CD $\overline{w'T_v'}$ magnitude is similar to that of the CU. However, not all fluxes are positive. Fluxes found within the upwind left and right bins, although not statistically significant, are counter-gradient. In contrast and as will be seen in sub-section 3.3., all fluxes composing the CD absolute humidity composite CU of this study are down-gradient. Keeping in mind the lack of statistical confidence, the upwind left and right bins of $\overline{w'T_v'}$ for the CD composite, then, depart from findings of Khalsa and Greenhut (1985) that warm dry downdrafts have negative buoyancy flux only at levels

TABLE IV

CD buoyancy flux composite and corresponding standard deviations.

$\overline{w'T_v'}$ (ms ⁻¹ °C) (std. dev.)	Left	Center	Right
Downwind	0.009 (0.005)	0.005 (0.001)	0.009 (0.005)
Middle	0.004 (0.001)	0.006	0.004 (0.001)
Upwind	-0.002 (0.009)	0.004 (0.001)	-0.002 (0.009)

higher than the surface layer. Similar to what is suggested in Khalsa and Greenhut (1985) for some of their anomalous patterns, the counter-gradient $\overline{w'T_v'}$ of this study may result from entrainment of buoyant CU air into the upwind side of the CD. The positive buoyancy flux portion of the CD $\overline{w'T_v'}$ composite of this study compares well with findings in the lowest levels of Khalsa and Greenhut (1985).

Of final note: a surface layer counter-gradient heat flux is found in the upwind region of the ensemble downdraft of Wilczak's (1984) vertical cross section. Thus, the finding of Wilczak (1984) compares well with the current study.

3.3. ABSOLUTE HUMIDITY FLUX

The planview CU absolute humidity flux composite is presented in Table V. Statistical confidence in $\overline{w'r'}$ exists

TABLE V

CU absolute humidity flux composite and corresponding standard deviations.

$\overline{w'r'}$ (gs ⁻¹ m ⁻²) (std. dev.)	Left	Center	Right
Downwind	0.045 (0.003)	0.041 (0.005)	0.045 (0.003)
Middle	0.039 (0.005)	0.068	0.041 (0.008)
Upwind	0.049 (0.003)	0.053 (0.010)	0.049 (0.003)

for all bins of the composite. As is expected by parcel displacement theory for a CMASL, flux in all bins of the composite is down-gradient. This property is also found in the majority of updrafts and downdrafts of Khalsa and Greenhut (1985). Composite patterns of $\overline{w'r'}$ resemble, for the most part, those of $\overline{w'w'}$. The largest flux magnitude is found in the middle center bin. Fluxes along the upwind side of the

draft is slightly larger than those on the downwind side. There is, however, symmetry along the cross-mean-wind group axis.

The CD $\overline{w'r'}$ composite is presented in Table VI. As with

TABLE VI

CD absolute humidity flux composite and corresponding standard deviations.

$\overline{w'r'}$ (gs ⁻¹ m ⁻²) (std. dev.)	Left	Center	Right
Downwind	0.025 (0.003)	0.025 (0.003)	0.025 (0.003)
Middle	0.023 (0.004)	0.034	0.022 (0.003)
Upwind	0.020 (0.002)	0.021 (0.002)	0.020 (0.002)

the CU, there is statistical confidence in the entire composite and the absolute humidity flux is down-gradient throughout the composite, with a maximum at the center. There are, however, some differences from the CU $\overline{w'r'}$ composite. As is expected from parcel displacement theory and the relative magnitudes of flux in the $\overline{w'w'}$ draft composites, a weaker absolute humidity flux composite is observed for the CD. Also,

the downwind side of the CD composite contains slightly stronger flux than that of the upwind side but as in the CU composite, symmetry exists along the cross-mean-wind group axis.

3.4 MOMENTUM FLUX

There is statistical confidence for all bins of the CU planview along-mean-wind momentum flux composite, presented in Table VII. The flux contained in all bins are down-gradient, given the usual sign of the surface layer wind shear. This same property is seen in moist updrafts by Khalsa and Greenhut (1985). Wilczak (1984), however, shows a region of counter-gradient momentum flux just inside the trailing edge of his ensemble updraft vertical cross section. The largest flux magnitude in the CU composite is found in the middle center bin. Less significant asymmetries exist. For example, $\overline{w'u'}$ is stronger along the downwind side of the composite than along the upwind side. Weakest flux is found in the middle left and right bins.

The CD planview flux composite of $\overline{w'u'}$ is presented in Table VIII. Statistical confidence exists in all data with

TABLE VII

CU along-mean-wind momentum flux composite and corresponding standard deviations.

$\overline{w'u'}$ (m ² s ⁻²) (std. dev.)	Left	Center	Right
Downwind	-0.133 (0.008)	-0.145 (0.041)	-0.133 (0.008)
Middle	-0.107 (0.016)	-0.219	-0.099 (0.018)
Upwind	-0.122 (0.023)	-0.123 (0.037)	-0.122 (0.023)

the exception of the upwind center bin, where the standard deviation approaches the magnitude of the flux. As with the CU, and as seen in Khalsa and Greenhut (1985), $\overline{w'u'}$ is down-gradient throughout the composite. As discussed below, this finding differs from that of Wilczak (1984) for his ensemble downdraft vertical cross section of $\overline{w'u'}$. The region of strongest flux within the CD composite is found on the downwind side, while weakest flux is on the upwind side. The largest magnitude of $\overline{w'u'}$ is seen in the downwind center bin while the smallest is in the upwind center bin. Cross-mean-wind group axis symmetry is seen.

As stated above, Wilczak (1984), using finer

observational resolution than was possible in this study, shows a region of counter-gradient momentum flux just inside

TABLE VIII

CD along-mean-wind momentum flux composite and corresponding standard deviations.

$\overline{w'u'}$ (m^2s^{-2}) (std. dev.)	Left	Center	Right
Downwind	-0.077 (0.014)	-0.092 (0.027)	-0.077 (0.014)
Middle	-0.065 (0.015)	-0.084	-0.063 (0.016)
Upwind	-0.043 (0.008)	-0.028 (0.022)	-0.043 (0.008)

the trailing edge of his ensemble updrafts and downdrafts. Given the differences in horizontal resolution, it is possible that the along-mean-wind asymmetries in both studies are related.

4. Summary

The coupling of the atmosphere to the ocean surface is accomplished predominately through fluxes induced by drafts within the marine atmospheric surface layer. Planview composite draft eddy correlation flux patterns of vertical velocity, buoyancy, absolute humidity, and the along-mean-wind component of momentum, within the convective marine atmospheric surface layer, are derived in this study. High resolution turbulence data are obtained from 20 NCAR Electra 50 m mean sea level flight legs from Project FIRE. Data processing results in a demeaned, detrended, despiked, high-pass filtered perturbation dataset.

A conditional sampling technique is used to isolate updrafts and downdrafts of interest from the environment. The technique uses horizontal scale and magnitude thresholds based on w' event criteria. The w' dataset is band-pass filtered to eliminate the inertial subrange contribution ($0.1 Z_i$ cutoff wavelength) and the mesoscale contribution ($1.5 Z_i$ cutoff wavelength). The minimum draft width is 50 m while 0.1 m/s is the w' magnitude threshold. This technique results in the isolation of 2839 updrafts, averaging 98 m in width, and 3062 downdrafts, averaging 107 m in width.

After the identification of drafts of interest, eddy correlation fluxes are calculated for those portions of the processed dataset where drafts of interest are located. Mean wind positioning within drafts, draft symmetry, and mean draft

intensity are used to implement a series of averaging calculations, grouping techniques, and scaling operations.

The result of the above data manipulation is a planview composite updraft and downdraft for each flux discussed. The composites are composed of flux data located in horizontal three bin by three bin arrays. Each bin represents a mean-wind-relative sector of a composite draft: upwind, middle, or downwind by left, center, or right. Along-mean-wind group axes extend through the center of composite drafts while cross-mean-wind group axes extend through the middle of composite drafts.

Statistical confidence exists in the two vertical velocity flux composites. The strongest flux region of the updraft composite is located along the along-mean-wind group axis, with the largest magnitude flux found at the center of the draft. While the largest magnitude of $\overline{w'w'}$ within the downdraft composite is also found at the center of the draft, the overall composite is weaker and more uniform than that of the updraft. In the buoyancy flux composites, only data in bins along the along-mean-wind and cross-mean-wind group axes are statistically significant. Along these axes, symmetries exist and the fluxes are down-gradient. Statistical confidence exists throughout both absolute humidity flux composites. As is expected by parcel displacement theory, all fluxes are down-gradient. The largest magnitudes of flux are found in the middle center bins, and both composites show cross-mean-wind group axis symmetry. The updraft and

downdraft along-mean-wind component of momentum flux composites are statistically significant throughout, with the exception of the upwind center bin of the downdraft composite. All fluxes of both composites are down-gradient. The largest flux magnitude for the updraft is in the middle center bin while that of the downdraft is located in the downwind center bin. Along-mean-wind asymmetry exists within both composites with downwind bins having greater magnitudes of flux than upwind bins.

It is hoped that this study provides new useful insight into the planview flux structure of CMASL updrafts and downdrafts. The degree of spatial resolution in these results, as well as the techniques presented in this study, could be of use in verification of nonlinear convective boundary layer models such as that presented in Haack and Shirer (1992). These results are also appropriate for the input of forcing in time dependent two-dimensional ocean wave models of cats paw-type features.

Of course much room exists for improvement upon and expansion beyond this study. This study should be used as a stepping stone for such research initiatives.

Acknowledgements

We would like to thank H. N. Shirer, S. J. S. Khalsa and K. A. Moyer for valuable discussions and suggestions. Also we would like to thank the anonymous reviewer for the very useful comments. The research reported in this work was funded by the Office of Naval Research under Grant N00014-90-J-4012.

References

- Albrecht, B. A., Randall, D. A., and Nicholls, S.: 1988, 'Observations of Marine Stratocumulus Clouds During FIRE', *Bull. Amer. Meteorol. Soc.* **69**, 618-626.
- Dorman, C. E. and Mollo-Christensen, E.: 1973, 'Observation of the Structure on Moving Gust Patterns Over a Water Surface ("Cat's Paws")', *J. Phys. Ocean.* **3**, 120-132.
- Gaynor, J. E., and Mandics, P. A.: 1978, 'Analysis of the Tropical Marine Boundary Layer During GATE Using Acoustic Sounder Data', *Mon. Wea. Rev.* **106**, 223-232.
- Geernaert, G. L., and Hansen, F.: 1992, 'Low Frequency Variability of the Wind Stress Vector in the Surface Layer Over the Sea', *Preprints Tenth Symp. on Turbulence and Diffusion*, Portland, Amer. Meteor. Soc.
- Greenhut, G. K., and Khalsa, S. J. S.: 1982, 'Updraft and Downdraft Events in the Atmospheric Boundary Layer Over the Equatorial Pacific Ocean', *J. Atmos. Sci.* **39**, 1803-1818.
- Haack, T., and Shirer, H. N.: 1992, 'Mixed Convective-Dynamic Vortices and Their Effects on Initial Wind and Temperature Profiles', *J. Atmos. Sci.* **49**, 1181-1201.
- Khalsa, S. J. S., and Greenhut, G. K.: 1985, 'Conditional Sampling of Updrafts and Downdrafts in the Marine Atmospheric Boundary Layer', *J. Atmos. Sci.* **42**, 2550-2562.
- Kloesel, K. A., Albrecht, B. A., and Wylie, D. P.: 1988, 'FIRE Marine Stratocumulus Observations-Summary of Operations and Synoptic Conditions', Penn State University, Department of Meteorology, FIRE Technical Report No. 1.
- Lenschow, D. H. and Stephens, P. L.: 1980, 'The Role of Thermals in the Convective Boundary Layer', *Boundary-Layer Meteorol.* **19**, 509-532.
- Liu, W.T., Katsaros, K.B., and Businger, J.A.: 1979, 'Bulk Parameterization of the Air-Sea Exchanges of Heat and Water Vapor Including the Molecular Constraints at the Interface', *J. Atmos. Sci.* **36**, 1722-1735.
- Moyer, K. A. and Young, G. S.: 1991, 'Observations of Vertical Velocity Skewness Within the Marine Stratocumulus-Topped Boundary Layer', *J. Atmos. Sci.* **48**, 403-410.
- Nucciarone, J. J. and Young, G. S.: 1991, 'Aircraft

- Measurements of Turbulence Spectra in the Marine Stratocumulus-Topped Boundary Layer', *J. Atmos. Sci.* **48**, 2382-2392.
- Schumann, U. and Moeng, C.-H.: 1991, 'Plume Fluxes in Clear and Cloudy Convective Boundary Layers', *J. Atmos. Sci.* **48**, 1746-1757.
- Sikora, T. D. and Young, G. S.: In Press, 'Observations of Planview flux Patterns Within Convective Structures of the Marine Atmospheric Surface Layer', *Boundary-Layer Meteorol.*
- Stull, R. B.: 1988, *An Introduction to Boundary Layer Meteorology*, Kluwer Academic Publishers, Dordrecht.
- Wilczak, J. M.: 1984, 'Large-Scale Eddies in the Unstably Stratified Atmospheric Surface Layer. Part I: Velocity and Temperature Structure', *J. Atmos. Sci.* **41**, 3537-3550.
- Wilczak, J. M. and Tillman, J. E.: 1980, 'The Three-Dimensional Structure of Convection in the Atmospheric Surface Layer', *J. Atmos. Sci.* **37**, 2424-2443.
- Woodcock, A. H.: 1940, 'Convection and Soaring Over the Open Sea', *J. Marine Res.* **3**, 248-253.
- Woodcock, A. H.: 1975, 'Thermals Over the Sea and Gull Flight Behavior', *Boundary-Layer Meteorol.* **9**, 63-68.
- Young, G. S.: 1987, 'Mixed Layer Spectra From Aircraft Measurements', *J. Atmos. Sci.* **44**, 1251-1256.
- Young, G. S.: 1988, 'Turbulence Structure of the Convective Boundary Layer. Part II: Phoenix 78 Aircraft Observations of Thermals and Their Environment', *J. Atmos. Sci.* **45**, 727-735.

APPENDIX B

**IMPROVED ALGORITHMS FOR
ESTIMATING THE CORRELATION
DIMENSION AND THE ASSOCIATED
PROBABLE ERRORS**

R. WELLS, H. N. SHIRER, C. FOSMIRE, J. A. DORAN

Departments of Mathematics and Meteorology

The Pennsylvania State University

January 1993

Abstract

The correlation dimension d is used commonly to quantify the chaotic structure of an attractor of a smooth dynamical system. The standard algorithm for estimating the value of d is based on finding the slope of the curve obtained by plotting $\ln C(r)$ versus $\ln r$, where $C(r)$ is the correlation integral and r is the distance between points on the attractor. It is argued here that this algorithm depends implicitly and sensitively on the assumption that $C(r)$ is differentiable, which is an assumption apparently not applicable to even the Lorenz attractor. Moreover, there is uncertainty in the value typically cited for d because its numerical approximation is often expressed as a function of r and because no objective criterion is given for locating the scaling region of appropriate values of r to consider. Finally, *a priori* statistical error bounds on the approximate value for d are typically not reported.

In this article, a rigorous means for obtaining from a single data set an *infinite number* of independent estimates for the correlation dimension d is given that relies only on the three assumptions that $C(r)$ is continuous, that $C(r)$ obeys the relation $C(r) \sim r^d$ as r approaches zero, and that a certain limiting moment exists. The most likely candidates for d given by this new integral method are those estimates that are relatively constant and close to one another in a range of r . Moreover, it is demonstrated that, when the nonlacunar relationship $C(r) = r^d$ holds but the empirical estimate $C_e(r)$ of $C(r)$ is poor for small values of r , the integral method converges more rapidly to the correct value of d than does the standard slope method. Validation of the estimates for d is obtained by making *a priori* statistical error estimates that crudely bound the errors between the approximate and actual values of d . The most likely value for d is now the one yielding the smallest error in these estimates. Although these results bear on the location of the scaling region, the problem of identifying that region remains open.

A rigorous probabilistic approach is used to develop the expressions in this article. For any positive numbers p and ρ , the expected value of $(r/\rho)^p$ over distances less than or equal to ρ is denoted by $E((r/\rho)^p : r \leq \rho)$. The limiting moment $M(p)$ is then defined to be the limit of this expected value as ρ approaches zero. An infinite number of estimates for d is obtained first by varying the value of p to produce different values of $M(p)$ and then by using the simple formula $d = pM(p)/(1 - M(p))$. *A priori* statistical estimates are given for the errors in the approximations of the expected values $E((r/\rho)^p : r \leq \rho)$. Coarser estimates are given for their differences from $M(p)$, and finally for the resulting approximations of d . Further refining the identification of the scaling region thus depends on improving the estimates of the difference $|E((r/\rho)^p : r \leq \rho) - M(p)|$.

In important cases, the limiting moment $M(p)$ may not exist. But the limit of $E((r/\rho)^p : r \leq \rho)$ along a suitable sequence $\rho = \rho_1, \rho_2, \rho_3, \dots$ does exist, and yields the dimension in the same way. It is a subject for future research to determine this sequence.

Illustrations using the Lorenz and Henon attractors are presented. The integral method alone yields the following candidates for d : For the Lorenz attractor, 2.08 or 2.09 is indicated; but for the Henon attractor, no single value is strongly indicated, although the values appear to fall in the range $1.21 \leq d \leq 1.27$. For the Lorenz attractor, insufficient independent time series points are used to yield usable error bounds for d ; but for the Henon attractor, enough are used to produce the estimate $d = 1.25 \pm 0.15$, which holds with a 97.5% probability and moment error tolerance of 0.02, and the estimate $d = 1.25 \pm 0.1$, which holds with an 90% probability and moment error tolerance of 0.01. All these values fall within the ranges typically reported for each attractor.

A simple procedure for estimating the value of d emerges from the statistical error analysis and its application to the Henon attractor: The optimum value for d is the particular candidate from the above calculation that minimizes the difference between the bounds a and A in the inequalities $a \leq C(r)/r^d \leq A$ that follow from the strong version of the relation $C(r) \sim r^d$, upon which the *a priori* statistical error estimates are based.

Finally, an equation for the limit as ρ approaches zero of $E((r/\rho)^p [\ln(r/\rho)]^\gamma : r \leq \rho)$ is found that generalizes to the case $C(r) \sim r^d$ those formulas given by Takens for the nonlacunar case $C(r) \sim ar^d$ when $p=0$ and $\gamma=1$ or $\gamma=2$. In addition, similar equations are found for the Hentschel and Procaccia generalized dimensions D_q with q an integer.

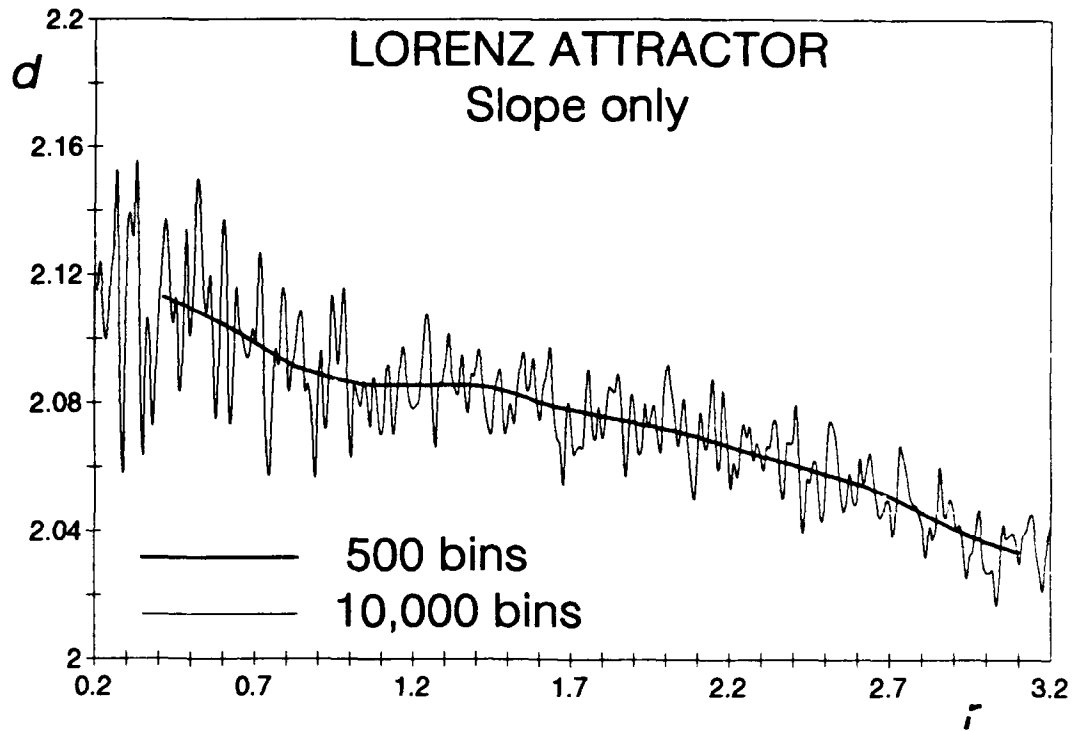
1. Introduction

Estimates of the correlation dimension d of a time series are commonly used for quantifying the chaotic complexity of a physical system (e.g., Grassberger and Procaccia, 1983a, b; Eckmann and Ruelle, 1985; Henderson and Wells, 1988; Baker and Gollub, 1990; Tsonis, 1992). However, owing to the presence of both intrinsic and extrinsic sources of error, the merits of this procedure have been debated considerably in the literature (e.g., Nicolis and Nicolis, 1984, 1987; Grassberger, 1986, 1987; Smith *et al.*, 1986; Theiler, 1986, 1988; Procaccia, 1988; Smith, 1988; Tsonis and Elsner, 1988, 1989, 1990; Nerenberg and Essex, 1990; Ruelle, 1990; Essex and Nerenberg, 1991).

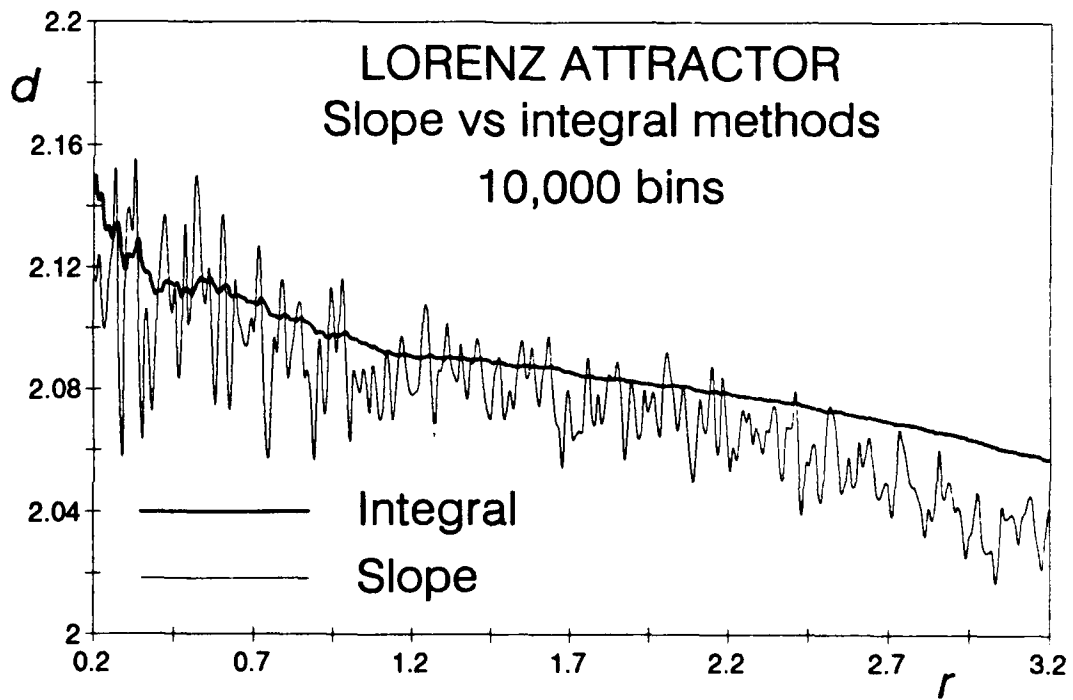
Numerous sources of error inherent in the approximation of the attractor dimension arise from such things as time series collection and preprocessing, model reconstruction, and the specific dimension algorithm used. Under time series collection, we include the frequency, number, continuity and duration of the measurements (Nicolis and Nicolis, 1984, 1987; Grassberger, 1986, 1987; Fraedrich, 1986; Smith *et al.*, 1986; Essex *et al.*, 1987; Smith, 1988; Keppene and Nicolis, 1989; Ramsey and Yuan, 1989; Nerenberg and Essex, 1990; Ruelle, 1990; Essex, 1991) and contamination by noise (Franaszek, 1984; Ben-Mizrachi *et al.*, 1984; Theiler, 1986; Simm *et al.*, 1987; Osborne and Provenzale, 1989; Theiler, 1991); under preprocessing, we include low or high pass filtering (Theiler, 1991), interpolation and trend removal, and principal component analysis (Albano *et al.*, 1988); under model reconstruction, we include the choice of variable or variables (Lorenz, 1991), embedding dimension (Mañé, 1981; Takens, 1981; Grassberger and Procaccia, 1983a, b; Keppene and Nicolis, 1989; Nerenberg and Essex, 1990; Tsonis *et al.*, 1993), and phase lag (Broomhead and King, 1986; Fraser and Swinney, 1986; Albano *et al.*, 1991; Thomson and Henderson, 1992); and under the dimension algorithm used, we include those proposed by Kaplan and Yorke (1979), Russell *et al.* (1980), Takens (1981), Greenside *et al.* (1982), Grassberger and Procaccia (1983a, b), Theiler (1987), Henderson and Wells (1988), and Kember and Fowler (1992).

In this article, we focus on the last general source, the dimension algorithm used. Thus it is a principal objective of this article to present, in section 2, new algorithms for sharpening the accuracy of the estimate for d . In deriving our new algorithms, we seek to avoid those errors that result from assuming that the correlation integral $C(r)$ is differentiable when it is not. For example, the standard *slope method*, which uses the slopes of the graph of $\ln C(r)$ versus $\ln r$ (e.g. Grassberger and Procaccia, 1983a, b; Nicolis and Nicolis, 1984; Eckmann and Ruelle, 1985; Fraedrich, 1986; Grassberger, 1986; Nese, 1987; Simm *et al.*, 1987; Henderson and Wells, 1988; Keppene and Nicolis, 1989; Tsonis and Elsner, 1989; Nerenberg and Essex, 1990; Albano *et al.*, 1991; Lorenz, 1991; Nerenberg *et al.*, 1991), rests implicitly on the hypothesis that $C(r)$ is differentiable.

Unfortunately, careful numerical analysis of the Lorenz attractor (Lorenz, 1963) suggests that $C(r)$ is *not* differentiable. In Figure 1a, two slope method estimates for d are shown that were each obtained using a simple three-point centered finite-difference approximation. So that problems introduced by employing model reconstruction of a single series (e.g., Takens, 1981) were not encountered, both these estimates are based on the same three-variable, transient-free time series of 20,000 points separated by a time interval of 0.5. In the first case, the distance data were partitioned into 500 bins of width 0.2, while in the second case, they were partitioned into 10,000 bins of width 0.01. In Figure 1a, the estimates for d using data up to bin distances r are shown; clearly, as the resolution is increased by decreasing the bin width, the estimates for d become noisier, thereby suggesting that the slopes of the correlation function are not approaching a limit; that is, the correlation function is not differentiable. Similar results can be inferred from those in Cutler (1991).

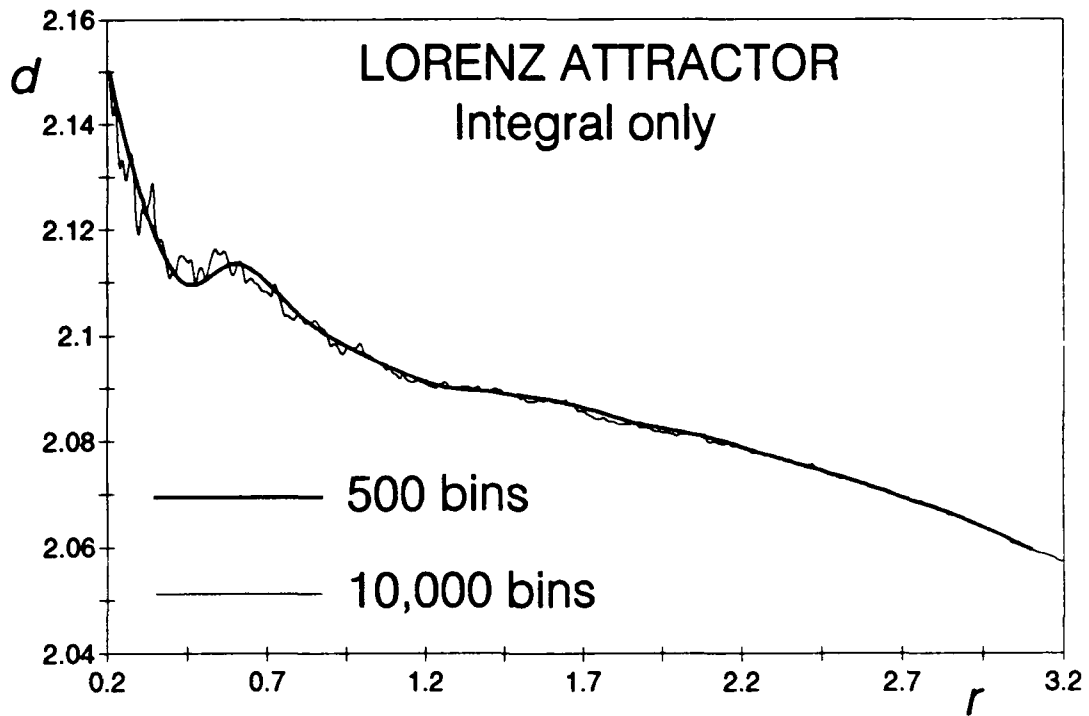


(a)



(b)

Figure 1



(c)

Figure 1. Estimates of the correlation dimension d for the Lorenz attractor. A transient-free, three-variable time series containing 20,000 points is used for the standard case of Rayleigh number $Ra = 28$, Prandtl number $\sigma = 10$, and domain shape parameter $b = 8/3$. In (a), the standard slope method is compared when 500 (thick curve; bin width 0.2) and 10,000 (thin curve; bin width 0.01) distance r bins are used; in (b) the slope (thin curve) and integral (thick curve; $p = 1$) methods are compared for the 10,000-bin case; and in (c) the integral method ($p = 1$) is compared using 500 (thick curve) and 10,000 (thin curve) bins.

If in fact the function $C(r)$ is not differentiable, then the standard slope procedure for estimating the value of d has no foundation and may well break down. We may illustrate such a collapse in the slope procedure by considering the middle-third Cantor set. In this case, the function $C(r)$ is the well-known Cantor function that is almost everywhere differentiable with derivative zero (Folland, 1984). For this function, the slope procedure, especially if perfectly implemented, would yield an estimate of zero for the correlation dimension d of the Cantor set rather than the correct value of $\ln 2/\ln 3$ (Mandelbrot, 1983; Barnsley, 1988; Cutler, 1991). The example of the Cantor function presents deeper problems as well: Theiler (1988) shows that the Takens (1985) formula fails to converge for this example, and below we note that Theiler's argument applies to show that our limiting moment $M(p)$ does not exist for the Cantor function. We believe that finding a rapidly converging algorithm for the Cantor function is an outstanding problem to solve in the search for improved dimension algorithms (see also Arneodo *et al.*, 1987).

In Figure 1b we compare results given by the slope method and the integral method introduced in this article. Both estimates for d use the same 20,000-point transient-free time series from the Lorenz model that was used to create Figure 1a, and both use distance data partitioned into 10,000 bins. As also illustrated in Figure 1c, our method clearly does not suffer from the same noisy property as does the slope method. Moreover, as discussed in section 3, our approach is not equivalent to merely averaging the slope estimates over some interval of r , and in fact gives a more accurate answer in an idealized case when there is noise contamination at small values of r .

We develop in section 2 an integral method that avoids the hypothesis that $C(r)$ is differentiable by integrating the product $r^p C(r)$; this method is a generalization of a dimension estimator proposed by Theiler (1988; 1990) that in turn is based on one proposed by Takens (1985). We compare in section 3 the accuracy of the integral method with that of the slope method in a particular case where $C(r)$ scales one way (r^c) in an undersampled or noise-contaminated region and another way (r^d) in a well-sampled region. For example,

Essex (1991) argues that undersampling leads to a value of c that is less than the correct value of the dimension. In contrast, Ben-Mizrachi *et al.* (1984) and Simm *et al.* (1987) argue that the dimension c to be expected from the noise-contaminated region is the embedding dimension, while the dimension from the well-sampled region is the correct one d . In our comparison in section 3, we find both analytically and numerically that the integral method converges much more rapidly to the correct dimension than does the slope method. In turn, Theiler (1988) notes that the slope method converges more rapidly than does direct application of the definition of the correlation dimension.

Another advantage of the integral method is that we may interpret it in a statistical way so that we are able, in section 5, to equip its dimension approximants with fairly natural *a priori* error estimates (*cf.*, Denker and Keller, 1986; Holzfuss and Mayer-Kress, 1986; Ramsey and Yuan, 1989; Theiler, 1990; Judd, 1992; Kember and Fowler, 1992). We apply in section 6 the integral method dimension and error estimates to the Henon attractor (Henon, 1976) and the Lorenz attractor (Lorenz, 1963).

Finally, in section 4 we develop rigorous generalizations of the Takens formulas for estimating the value of d (Takens, 1985) and in section 7 we derive a variant of the integral method for the Hentschel-Procaccia generalized dimensions D_q with q an integer (Hentschel and Procaccia, 1983). Concluding remarks in section 8 finish the article.

2. Integral Method for Estimating d

We recall the *slope method* for extracting the correlation dimension d from knowledge of the correlation integral $C(r)$. First, we suppose that we have the asymptotic relation

$$C(r) \sim r^d \tag{2.1}$$

defining the dimension d . It follows immediately that the limit equation

$$d = \lim_{r \rightarrow 0} \frac{\ln C(r)}{\ln r} \quad (2.2)$$

produces d . Unfortunately, using (2.2) is an inefficient way to find d (Theiler, 1988); but in the case that $C(r)$ is *differentiable*, we may apply L'Hôpital's Rule to (2.2) to obtain the more efficient formula (Theiler, 1986; Albano *et al.*, 1988)

$$d = \lim_{r \rightarrow 0} \frac{d \ln C(r)}{d \ln r} = \lim_{r \rightarrow 0} \frac{r}{C(r)} \frac{dC(r)}{dr} \quad (2.3)$$

Unfortunately again, if $C(r)$ is not known to be differentiable, then the transition from (2.2) to (2.3) is not necessarily valid and (2.3) does not make sense. Furthermore, even if $C(r)$ is differentiable, L'Hôpital's Rule may *not* apply to make the two limits in (2.3) equal. Accordingly, we need an alternative algorithm in the nondifferentiable case.

In this section we develop such an algorithm. We begin by regarding the correlation integral $C(r)$ as a cumulative probability distribution for the random variable r . Consequently, we may define for any positive number ρ the p th *normalized moment relative to the condition* $r \leq \rho$ as the expected value $E\left((r/\rho)^p : r \leq \rho\right)$ of the random variable $(r/\rho)^p$, subject to the condition $r \leq \rho$. Thus, we set

$$E\left((r/\rho)^p : r \leq \rho\right) = \frac{1}{C(\rho)} \int_0^\rho \left(\frac{r}{\rho}\right)^p dC(r) \quad (2.4)$$

Then we define the p th *limiting moment* $M(p)$ of $C(r)$ by setting

$$M(p) = \lim_{\rho \rightarrow 0} E\left((r/\rho)^p : r \leq \rho\right) \quad (2.5)$$

The basic result of this section is that, if the limit in (2.5) exists, then the equation

$$d = \frac{pM(p)}{1 - M(p)} \quad (2.6)$$

is valid for the correlation dimension d given by (2.2).

To see that (2.6) is valid, we find it helpful to interpret the asymptotic relation (2.1) in two senses, a *strong sense* and a *weak sense*. We say that (2.1) holds in the strong sense if there exist positive numbers a , A , and ρ_0 for which the inequalities

$$a \leq C(r)/r^d \leq A \quad (2.7)$$

hold whenever the value of r satisfies

$$0 \leq r \leq \rho_0 \quad (2.8)$$

The numbers a , A , and ρ_0 are parameters relevant to the statistical error estimates in section 5, where we must therefore require the strong sense. We note that the case $a = A$ is the one termed *nonlacunar* by Theiler (1988).

In contrast, we say that (2.1) holds in the *weak sense* if the limit equations

$$\lim_{r \rightarrow 0} \frac{C(r)}{r^{d_1}} = 0 \quad (2.9)$$

and

$$\lim_{r \rightarrow 0} \frac{C(r)}{r^{d_2}} = \infty \quad (2.10)$$

are valid for any two numbers d_1 and d_2 satisfying

$$d_1 < d < d_2 \quad (2.11)$$

Of course, the strong sense implies the weak. It is the weak sense that suffices for the derivation below of the formulas for our new integral method.

We need to make only three assumptions about the function $C(r)$, assumptions we believe to be commonly made and reasonable when $C(r)$ is the correlation integral:

- (i) We assume that $C(r)$ is a continuous function of r . That is, we assume that no particular value of r is realized with positive probability.
- (ii) We assume that the asymptotic equation $C(r) \sim r^d$ holds in the weak sense.
- (iii) For some value of $p \neq 0$ such that $d + p > 1$, we assume that the limiting moment $M(p)$ of (2.5) exists.

The argument that these three assumptions yield (2.6) is embodied in an easy calculation. First we integrate by parts to obtain

$$\int_0^\rho r^p dC(r) = \rho^p C(\rho) - p \int_0^\rho r^{p-1} C(r) dr \quad (2.12)$$

We combine (2.12) with the definition (2.4) to find

$$E\left(\left(\frac{r}{\rho}\right)^p : r \leq \rho\right) = 1 - p \frac{\int_0^\rho r^{p-1} C(r) dr}{\rho^p C(\rho)} \quad (2.13)$$

Therefore, because the limit $M(p)$ exists by assumption (iii), we obtain

$$M(p) = 1 - p \lim_{\rho \rightarrow 0} \frac{\int_0^\rho r^{p-1} C(r) dr}{\rho^p C(\rho)} \quad (2.14)$$

in which it follows that the limit on the right side exists. Next we verify that we have

$$\int_0^\rho r^{p-1} C(r) dr \sim \rho^{p+d} \quad (2.15)$$

in the weak sense, from which it follows that

$$p + d = \lim_{\rho \rightarrow 0} \frac{\ln \int_0^\rho r^{p-1} C(r) dr}{\ln \rho} \quad (2.16)$$

Because we have assumed that $d + p > 1$, we see that the function $r^{p-1} C(r)$ of r is continuous, and then that $\int_0^\rho r^{p-1} C(r) dr$ is a *differentiable* function of ρ . Consequently, we may apply L'Hôpital's Rule to obtain

$$p+d = \lim_{\rho \rightarrow 0} \frac{\rho^p C(\rho)}{\int_0^\rho r^{p-1} C(r) dr} \quad (2.17)$$

in which the limit exists by (2.14) and assumption (iii). Finally, we obtain from (2.14) and (2.17)

$$M(p) = 1 - p \frac{1}{p+d} = \frac{d}{p+d} \quad (2.18)$$

from which (2.6) follows.

We note that in the case $p = 0$, the same Stieltjes integration by parts argument leads to the Takens estimator (Takens, 1985)

$$\frac{1}{C(\rho)} \int_0^\rho \frac{1}{r} dC(r) = -E([\ln(r/\rho)]: r \leq \rho) = \frac{1}{d} \quad (2.19)$$

which is essentially the content of (2.15) and (2.16) in Theiler (1988) or of (22) and (23) in Theiler (1990).

Remark 1. There is an important subtlety at this point: L'Hôpital's Rule does *not* imply that if the limit in (2.16) exists, then so does $M(p)$. In fact, the limit in (2.16) exists whenever $C(r) \sim r^d$ holds, even in the case $p = 0$, but, as Theiler (1988) notes, the corresponding moment $M(0,1)$ defined in (4.19) does *not* exist for $C(r)$ the Cantor function; accordingly, the Takens estimator (2.19) fails in that case. In fact, Theiler's argument applies to show that also the limit $M(p)$ fails to exist for $C(r)$ the Cantor function.

Remark 2. Even if the limit in (2.17) fails to exist, the Cauchy Mean Value Theorem (used to prove L'Hôpital's Rule; James, 1967) implies that there exists a sequence $\rho_1, \rho_2, \rho_3, \dots$ of values of ρ converging to zero, so that the limit

$$M_s(p) = \lim_{k \rightarrow \infty} E((r/\rho_k)^p : r \leq \rho_k) \quad (2.20)$$

exists. Then the correlation dimension is given by

$$d = \frac{pM_s(p)}{(1 - M_s(p))} \quad (2.21)$$

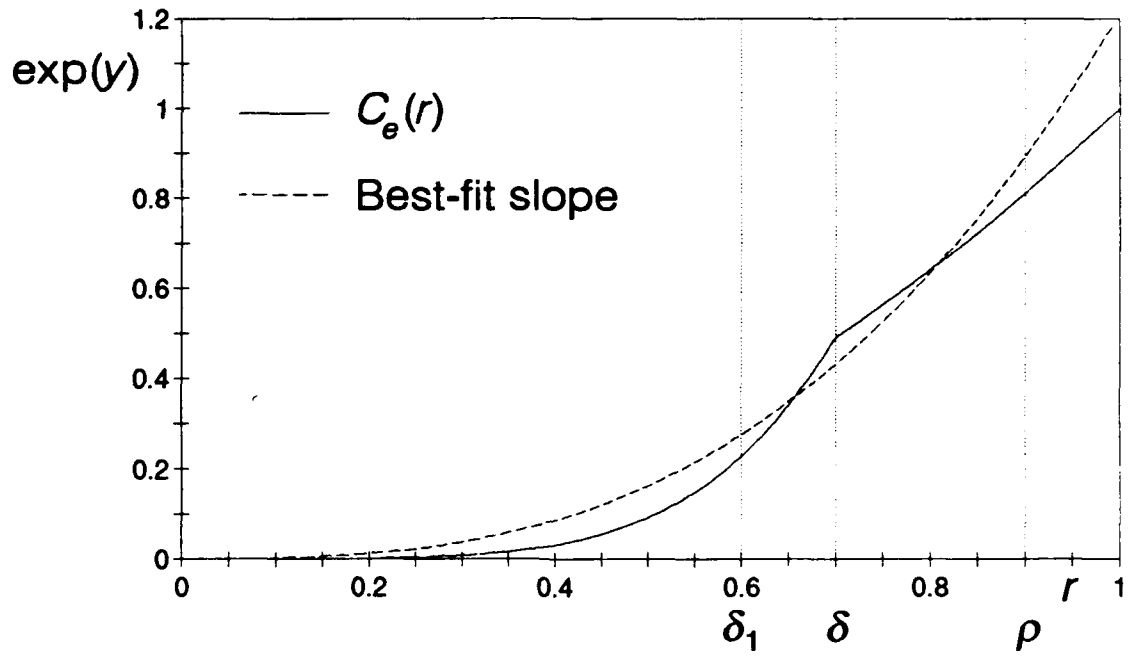
3. Comparison of Slope and Integral Methods for Estimating d

To form some idea of the relative accuracies of the slope and integral methods, we consider a case in which the nonlacunar correlation integral $C(r)$ is approximated by the empirical correlation function

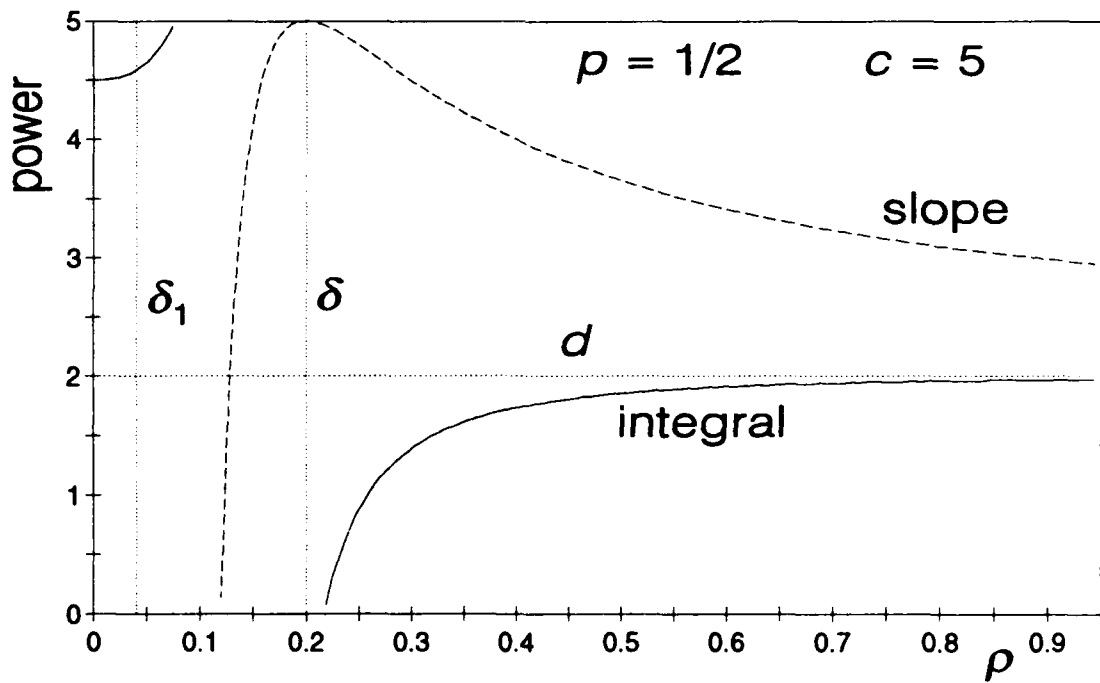
$$C_e(r) = \begin{cases} \delta^{d-c} r^c & \text{for } 0 \leq r \leq \delta \\ r^d & \text{for } \delta \leq r \leq \rho \end{cases} \quad (3.1)$$

where δ is a positive number; this function is given by the solid curve in Figure 2a.

We take (3.1) as a paradigm for the common situation in which small amplitude noise distorts the empirical determination of the correlation integral $C(r)$ for small values of r . In the idealized situation represented by (3.1), we postulate that we recover $C(r)$ perfectly for values of r in the range $\delta \leq r \leq \rho$, while small amplitude noise leads to a growth exponent c different from the actual value d in the range $0 \leq r \leq \delta$. Ben-Mizrachi *et al.* (1984), Simm *et al.* (1987) and Theiler (1986, 1991) have argued that an empirically determined correlation function may be expected to scale as r^c , with c the embedding dimension, for small values of r where noise contamination dominates, and as r^d , with d the correlation dimension, for larger values of r . Thus, following these studies, we select $c > d$ as the most realistic case for our example. The choice $c = 2d + 1$ (Mañé, 1981; Takens, 1981) guides our illustration of $C_e(r)$ in Figure 2a with $d = 2$ and $c = 5$.

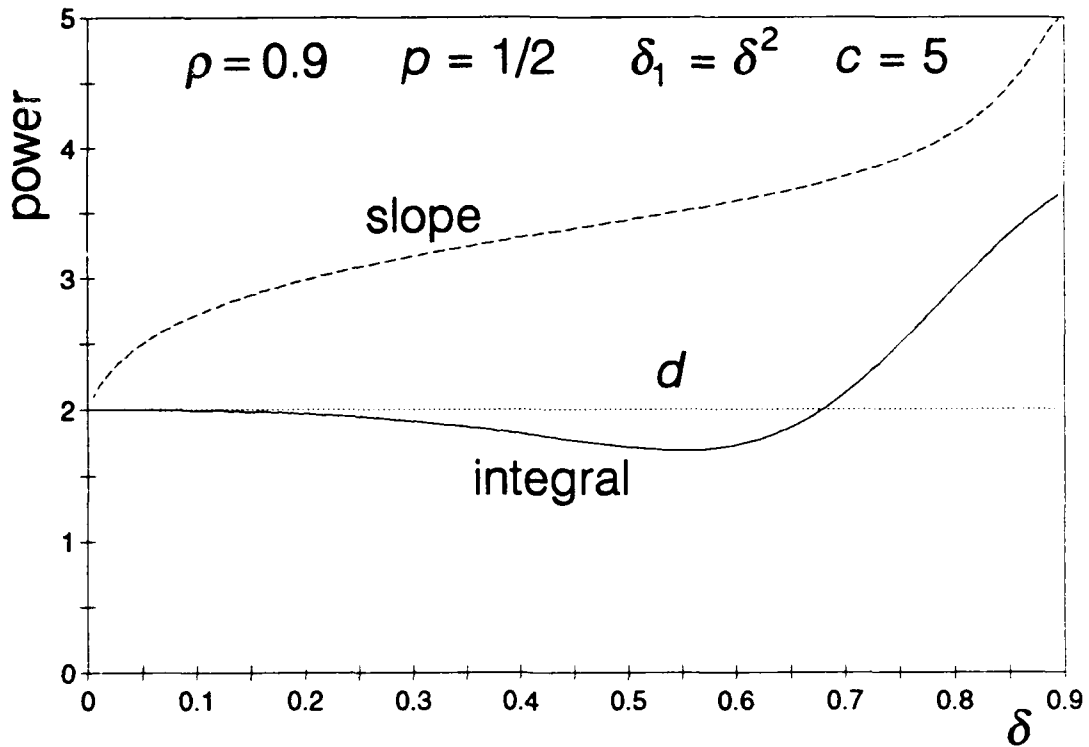


(a)



(b)

Figure 2



(c)

Figure 2. Comparison of slope and integral methods for the nonlacunar case $C(r) = r^d$ that is approximated by the empirical correlation function $C_e(r)$ in (3.1), with $d = 2$ and $c = 5$. Data are well sampled in the working interval $[\delta_1, \rho]$, but are noise-contaminated in the interval $[\delta_1, \delta]$. In (a), $C_e(r)$ (solid curve) and the curve for the best-fit slope $m(\delta_1, \rho)$, (3.4), (dashed curve) are shown for the case $\delta_1 = 0.6$, $\delta = 0.7$, and $\rho = 0.9$. In (b) and (c), the approximate dimensions given by the slope $m(\delta_1, \rho)$, (3.4), (dashed curve) and integral $d(p, \delta_1, \rho)$, (3.9), (solid curve) methods are compared. In (b), the case $\delta_1 = 0.04$, $\delta = 0.2$, and $p = \frac{1}{2}$ is illustrated as a function of ρ . In (c), the case $\delta_1 = \delta^2$, $p = \frac{1}{2}$, and $\rho = 0.9$ is shown as a function of δ . In both these cases, the integral method converges faster and is less sensitive to noise contamination than is the slope method.

Of course, in actual cases, there will be an intermediate region in which the empirical correlation function varies from being completely inaccurate for small values of r , to being essentially accurate for larger values of r . In our example, we eliminate this intermediate region for simplicity of calculation: The noise-dominated region gives way abruptly to the well-sampled region at $r = \delta$. Again, in actual cases, there seems to be no algorithm—or even advice—for deciding where the noise-dominated region ends and the well-sampled region begins. We incorporate this fact into our example below by not allowing knowledge of the value of δ to enter into our line fitting or integrating procedures; we use the value of δ only to evaluate the result of these procedures. However, we consider that the working interval $[\delta_1, \rho]$ of r used to approximate $C(r)$ includes both well-sampled and noise-dominated regions. Thus we hypothesize that the inequalities

$$0 < \delta_1 < \delta < \rho < 1 \quad (3.2)$$

are valid; the left-most inequality represents the fact that in any sampling of a time series, there is a smallest positive distance δ_1 . We expect, of course, that the accuracy of each calculation will improve as the length δ of the error-contaminated interval $[0, \delta]$ decreases in comparison with the length of the working interval $[\delta_1, \rho]$. Slightly more roughly, we expect the accuracy to improve as δ/ρ decreases in magnitude. Thus, we compare the slope and integral methods by discovering the rate at which this accuracy increases as the magnitude of δ/ρ decreases.

To implement the slope method in the standard way, we calculate the slope m of the line $y = m \ln r + b$ that best fits the curve $y = \ln C_e(r)$ between $r = \delta_1$ and $r = \rho$ in $y - \ln r$ space (Holzfuss and Mayer-Kress, 1986). If we measure the closeness of fit by means of the mean-square integral

$$I(m, b) = \int_{\delta_1}^{\rho} (m \ln r + b - \ln C_e(r))^2 dr \quad (3.3)$$

then we find that the value $m = m(\delta_1, \rho)$, belonging to the minimum of $I(m, b)$, is given, with the help of the symbolic manipulator Derive, by

$$m(\delta_1, \rho) = d + \frac{d-c}{\frac{\delta_1}{\rho} \left(\ln \frac{\delta_1}{\rho} \right)^2 - \left(1 - \frac{\delta_1}{\rho} \right)^2} \left[\left(\frac{\delta}{\rho} - \frac{\delta_1}{\rho} \right) \left(1 - \frac{\delta_1}{\rho} - \ln \frac{\delta}{\rho} \right) + \frac{\delta_1}{\rho} \ln \frac{\delta_1}{\delta} \left(1 - \frac{\delta}{\rho} - \ln \frac{\delta_1}{\rho} \right) \right] \quad (3.4)$$

This fit is illustrated by the dashed curve $\exp y = r^{m(\delta_1, \rho)} \exp b$ in Figure 2a.

Subject to the condition that there exist two numbers K_1 and K_2 so that

$$0 < K_1 \leq \delta_1/\delta \leq K_2 < 1 \quad (3.5)$$

holds, we obtain from (3.4) the asymptotic relation

$$m(\delta_1, \rho) - d = O\left(\frac{\delta}{\rho} \ln \frac{\delta}{\rho}\right) \quad (3.6)$$

Of course, when $\delta_1 = \delta$ we obtain from (3.4) the expected equality $m(\delta_1, \rho) - d = 0$. However, so long as our fitting interval $[\delta_1, \rho]$ is contaminated, even slightly, by the noise-dominated region, the difference between the approximate dimension $m(\delta_1, \rho)$, obtained from the slope method, and the actual dimension d approaches zero only at the rate of $(\delta/\rho) \ln(\delta/\rho)$ as the ratio δ/ρ approaches zero.

The rate of convergence as either ρ or δ varies is illustrated in Figures 2b, c, in which the approximate dimension $m(\delta_1, \rho)$ is denoted by the dashed curves. In Figure 2b, δ and δ_1 are held fixed and the approach of $m(\delta_1, \rho)$ to d shown as the value of ρ increases. In Figure 2c, ρ is held fixed with $\delta_1 = \delta^2$, and the approach of $m(\delta_1, \rho)$ to d illustrated as $\delta \rightarrow 0$. In both cases, the convergence is seen to be quite slow, meaning that even a small interval of r in which there is noise contamination introduces a considerable error in the slope dimension estimate.

In contrast, the difference between the approximate dimension obtained from the integral method and the actual dimension d approaches zero much faster, at least when the sum $p+d$ is greater than 1, as required by assumption (iii) in section 2. More specifically, we use as the interval of integration the same working interval as above, $[\delta_1, \rho]$, and we use the formula

$$M(p, \delta_1, \rho) = \frac{1}{C_e(\rho)} \int_{\delta_1}^{\rho} \left(\frac{r}{\rho}\right)^p dC_e(r) \quad (3.7)$$

to define the corresponding approximate p th moment $M(p, \delta_1, \rho)$. Then we use (2.6) to define the corresponding approximate dimension $d(p, \delta_1, \rho)$ as

$$d(p, \delta_1, \rho) = \frac{pM(p, \delta_1, \rho)}{1 - M(p, \delta_1, \rho)} \quad (3.8)$$

We see immediately with the help of Derive that we have

$$d(p, \delta_1, \rho) = d + (p+d) \frac{p(d-c) \left(\frac{\delta}{\rho}\right)^{p+d} + c(p+d) \left(\frac{\delta}{\rho}\right)^{d-c} \left(\frac{\delta_1}{\rho}\right)^{p+c}}{p(p+c) + p(d-c) \left(\frac{\delta}{\rho}\right)^{p+d} + c(p+d) \left(\frac{\delta}{\rho}\right)^{d-c} \left(\frac{\delta_1}{\rho}\right)^{p+c}} \quad (3.9)$$

so that

$$d(p, \delta_1, \rho) - d = o\left(\left(\frac{\delta}{\rho}\right)^{p+d}\right) \quad (3.10)$$

Thus, as the ratio δ/ρ approaches zero, we find that the integral approximate dimension $d(p, \delta_1, \rho)$ approaches the actual dimension d much faster than the slope approximate dimension $m(\delta_1, \rho)$ (3.4) does when $p+d > 1$ holds. This rapid approach is similar in spirit to that of Theiler (1988) who noted that his integral method, which is similar to ours for $p=0$, converges more rapidly than the slope method to the actual dimension as $\rho \rightarrow 0$. For

$p \neq 0$, the rapid approach is illustrated by the solid curves in Figures 2b, c for the conservative case $p = \frac{1}{2}$. Finally, we note from Figure 2b that if we interpret the interval $[\delta_1, \delta]$ as an undersampled region, then we obtain an underestimate for d in that region, in agreement with Essex (1991).

In contrast to the slope method, we note that the integral method yields an error in the approximate dimension $d(p, \delta_1, \rho)$ even when there is perfect sampling in the range $[\delta_1, \rho]$ because the integral (3.7) upon which the dimension estimate is based really should be calculated over the entire range $[0, \rho]$. Thus the limiting value of $d(p, \delta_1, \rho)$ when $\delta = \delta_1$ and $c = d$ is not d but

$$d(p, \delta_1, \rho) = d + (p+d) \frac{d \left(\frac{\delta}{\rho} \right)^{p+d}}{p+d \left(\frac{\delta}{\rho} \right)^{p+d}} \quad (3.11)$$

However, this result does not affect the conclusion given by (3.10) concerning the convergence rate as the noise-dominated region shrinks in size.

4. Extension of Moment Formulas to Those of Takens

In this section we derive the family of formulas given by

$$\lim_{\rho \rightarrow 0} E\left((r/\rho)^p [\ln(r/\rho)]^y : r \leq \rho\right) = (-1)^y \frac{d\gamma!}{(p+d)^{\gamma+1}} \quad (4.1)$$

Takens (1985) obtained the two estimators

$$\lim_{\rho \rightarrow 0} E([\ln(r/\rho)] : r \leq \rho) = -\frac{1}{d} \quad (4.2)$$

and

$$\lim_{\rho \rightarrow 0} E([\ln(r/\rho)]^2 : r \leq \rho) = \frac{2}{d^2} \quad (4.3)$$

for the special case of a nonlacunar correlation function $C(r)$ that scales perfectly with r ; that is, $C(r) = ar^d$. Here we extend (4.2) and (4.3) to all of (4.1) by deriving (4.1) for the general case $C(r) \sim r^d$, where we interpret this asymptotic relation in the weak sense defined in section 2.

We begin our derivation by noting that we may interpret some of the calculations of section 2 as describing the effect of rescaling on suitable measures on $[0, 1]$. We suppose that μ is a nonatomic probability measure on $[0, 1]$ with the property that every neighborhood of 0 in $[0, 1]$ has positive μ -measure. A particular example is the measure ν_d defined by setting

$$\nu_d(X) = d \int_X s^{d-1} ds \quad (4.4)$$

where X is a Borel subset of $[0, 1]$. Given such a measure μ , for any value of ρ satisfying

$$0 < \rho \leq 1 \quad (4.5)$$

we may define another such measure μ_ρ by setting

$$\mu_\rho(X) = \frac{\mu(\rho X)}{\mu[0, \rho]} \quad (4.6)$$

Using this notation, we may formulate an easy theorem:

Theorem If μ is a nonatomic probability measure satisfying the condition

$$C(\rho) = \mu[0, \rho] \sim \rho^d \quad (4.7)$$

for small values of ρ and possessing limiting moment $M(p)$ for $p = 0, 1, 2, \dots$, then the limit equation

$$\lim_{\rho \rightarrow 0} \mu_\rho = \nu_d \quad (4.8)$$

is valid in the weak topology for probability measures.

PROOF We calculate the moment $\int s^p d\mu_\rho(s)$ of the measure μ_ρ . We have

$$\int s^p d\mu_\rho(s) = \frac{1}{C(\rho)} \int_0^\rho \left(\frac{r}{\rho}\right)^p dC(r) \quad (4.9)$$

in which $s = r/\rho$ and $d\mu_\rho(s) = dC(r)/C(\rho)$. Consequently, we may use (2.4), (2.5) and (2.18) to obtain

$$\lim_{\rho \rightarrow 0} \int s^p d\mu_\rho(s) = \frac{d}{d+p} \quad (4.10)$$

However, for our standard measure ν_d , we see easily that

$$\int s^p d\nu_d(s) = \frac{d}{d+p} \quad (4.11)$$

for any value of $p \geq 0$. In particular, we have

$$\lim_{\rho \rightarrow 0} \int s^p d\mu_\rho(s) = \int s^p d\nu_d(s) \quad (4.12)$$

Consequently we find, for any polynomial $P(s)$, that

$$\lim_{\rho \rightarrow 0} \int P(s) d\mu_\rho(s) = \int P(s) d\nu_d(s) \quad (4.13)$$

and therefore for any continuous function $f(s)$, that

$$\lim_{\rho \rightarrow 0} \int f(s) d\mu_\rho(s) = \int f(s) d\nu_d(s) \quad (4.14)$$

Then, by definition of the topology on the space of Borel measures on $[0, 1]$, we have

$$\lim_{\rho \rightarrow 0} \mu_\rho = \nu_d \quad (4.15)$$

□

As a corollary of this theorem (which actually is the next-to-last step in its proof), we obtain the limit equation

$$\lim_{\rho \rightarrow 0} \int f(s) d\mu_{\rho}(s) = \int f(s) dv_d(s) = d \int_0^1 f(s) s^{d-1} ds \quad (4.16)$$

that is valid for any continuous function $f(s)$. Noting that

$$E(f(r/\rho): r \leq \rho) = \int f(s) d\mu_{\rho}(s) \quad (4.17)$$

holds, we obtain

$$\lim_{\rho \rightarrow 0} E(f(r/\rho): r \leq \rho) = d \int_0^1 f(s) s^{d-1} ds \quad (4.18)$$

Now, with $f(s) = s^p (\ln s)^{\gamma}$ and $p+d > 1$, we finally obtain the extension of the Takens (1985) formula for a generalized limiting moment:

$$M(p, \gamma) = \lim_{\rho \rightarrow 0} E\left(\left(\frac{r}{\rho}\right)^p [\ln(r/\rho)]^{\gamma} : r \leq \rho\right) = d \int_0^1 s^p [\ln s]^{\gamma} s^{d-1} ds = (-1)^{\gamma} \frac{d\gamma!}{(p+d)^{\gamma+1}} \quad (4.19)$$

This equation yields our formula (2.18) in the case $\gamma = 0$ and includes the Takens (1985) formulas as the cases $p = 0, \gamma = 1$ and $p = 0, \gamma = 2$, which are given by (4.2) and (4.3).

In practice, as outlined in Takens (1985), (4.2) gives us a way to estimate the value of d as a mean of a random sample, while (4.3) gives us a way to estimate the associated variance by means of the Kolmogorov Inequality. In the following section we make use of the parallel observation for $E\left(\left(\frac{r}{\rho}\right)^p : r \leq \rho\right)$ to arrive at statistical error estimates.

5. A Statistical Relative Error Bound for d

Takens (1985) notes that the special case $p=0$, $\gamma=1$ of (4.19) (essentially) expresses the mean of a random variable with variance (essentially) expressed by the special case $p=0$, $\gamma=2$. He also observes that it is therefore possible to incorporate statistical methods into an algorithm for estimating the value of the correlation dimension d . More recently, Theiler (1990) and Kember and Fowler (1992) use such methods to determine statistical error bounds on d .

Here we seek *a priori* statistical error bounds for estimates of the correlation dimension d given by the integral method. We first apply the conventional use of mean and variance to obtain quick but probably unreliable error bounds. Then we derive more reliable error bounds with the objective of identifying explicitly—and thereby making computationally accessible—the underlying assumptions necessary to derive such bounds.

To apply our knowledge of mean and variance to find conventional error bounds for an estimate of d , we envision a situation in which we may make a large number n of observations of the random variable $(r/\rho)^p$ for a fixed value of ρ . We *assume* that the value of ρ is so small that the value of $E((r/\rho)^p : r \leq \rho)$ is essentially indistinguishable from that of $M(p)$ so that we may interchange $M(p)$ and $E((r/\rho)^p : r \leq \rho)$ in our calculations. Then we may regard $M(p)$ as the expected value of our random variable $(r/\rho)^p$, and so regard $V(p) = M(2p) - M(p)^2$ as its variance. We next *assume* that our n observations are independent so that the mean of these observations has a variance of $V(p)/n$. Using the Central Limit Theorem (Feller, 1966), we know that when the value of n is large enough, the mean of n independent observations is essentially normally distributed; we therefore *assume* that in our case, the value of n is this large.

Accordingly, the 95% confidence interval J for $M(p)$ is given by

$$J = \left[M(p) - 2\sqrt{V(p)/n}, M(p) + 2\sqrt{V(p)/n} \right] \quad (5.1)$$

Using (2.18) for $M(p)$, we may rewrite (5.1) as

$$J = \left[\frac{p}{p+d} \left(1 - 2 \sqrt{\frac{d}{n(2p+d)}} \right), \frac{p}{p+d} \left(1 + 2 \sqrt{\frac{d}{n(2p+d)}} \right) \right] \quad (5.2)$$

Thus we conclude that, with ρ sufficiently small and n sufficiently large, the probability is 0.95 that the mean of n independent observations of $(r/\rho)^p$ is within a relative error of $\pm 2\sqrt{p^2/[nd(2p+d)]}$ of the actual value of $M(p)$. Then, upon applying (2.6) to our estimate (5.2) of $M(p)$, we find, with probability 0.95, the value of the correlation dimension d within a relative error of $\pm 2\sqrt{(p+d)^2/[nd(2p+d)]}$. For example, if we have $d=2$, $p=3$ and $n=10^6$, then we should recover d within a relative error of ± 0.0025 , so that $d = 2 \pm 0.005$, with probability approximately 0.95. Of course, such high precision is not attainable in practice (e.g., Fig. 1c; Grassberger and Procaccia, 1983a, b; Abraham *et al.*, 1986; Nese *et al.*, 1987; and Simm *et al.*, 1987).

The failure of conventional means to give realistic error bounds for an estimate of the correlation dimension suggests strongly that the values of ρ normally used are not sufficiently small to allow us to interchange such quantities as $M(p)$ and $E((r/\rho)^p : r \leq \rho)$, that the observations of quantities such as $(r/\rho)^p$ are not sufficiently independent to allow us to simply divide the variance of the mean by the number n of observations, or that the number of independent observations is not sufficiently large to justify our appeal to the Central Limit Theorem. Of these three difficulties, perhaps the most serious is the first, that ρ is not small enough, as emphasized by Caswell and Yorke (1986).

In view of these difficulties, we use much more elementary and direct, but laborious, methods in the remainder of this section to obtain realistic *a priori* statistical relative error bounds for the estimates of d given by the integral method. That is, for d_a an approximation obtained in a canonical way from a sample of the attractor, we find a formula bounding below the probability that the inequality

$$\left| \frac{d - d_a}{d} \right| \leq \epsilon \quad (5.3)$$

holds. In our derivation of that probability formula, we find it convenient to alter the usual definition of the function $C(r)$ to an essentially equivalent definition. In the usual definition, we consider a generic trajectory x_1, x_2, x_3, \dots of points on the attractor. For k any positive integer, we calculate the distances $|x_i - x_j|$ for $i < j < k$, and we let these distances be r_1, r_2, \dots, r_n , in order of calculation, with

$$n = \frac{k(k-1)}{2} \quad (5.4)$$

We set

$$C_k(r) = \frac{2}{k(k-1)} \text{card}\{(i, j) \mid |x_i - x_j| \leq r \text{ and } i < j < k\} \quad (5.5)$$

where $\text{card}(X)$ denotes the number of points in set X . Because the sequence x_1, x_2, x_3, \dots is generic, we may assume that the limit

$$C(r) = \lim_{k \rightarrow \infty} C_k(r) \quad (5.6)$$

exists and so defines the correlation function $C(r)$. In our altered definition, we consider a generic *pair* of trajectories x_1, x_2, \dots and y_1, y_2, \dots , and we define the time series r_1, r_2, \dots of distances by setting $r_i = |x_i - y_i|$. Then we redefine

$$C_n(r) = \frac{1}{n} \text{card}\{i \mid r_i \leq r \text{ and } i < j < n\} \quad (5.7)$$

and

$$C(r) = \lim_{n \rightarrow \infty} C_n(r) \quad (5.8)$$

This view is more convenient because we need not renumber the series r_1, r_2, \dots, r_n for $n = k(k-1)/2$ with each successive choice of k . More important is the fact that this interpretation avoids the implicit dependence via triangle inequalities of the distances $|x_i - x_j|$ (Theiler, 1990); this interpretation also makes it possible below to measure the near

independence of the distances r_i by means of autocorrelation. However, the two views are equivalent and our results below using the altered definition hold also for the original one.

For each value of ρ , we define the number $N(\rho, n)$ of distances less than ρ by setting

$$N(\rho, n) = \sum_{i=1}^n \chi(r_i/\rho) \quad (5.9)$$

where $\chi(\xi)$ is the characteristic function defined by

$$\chi(\xi) = \begin{cases} 1 & \text{if } |\xi| \leq 1 \\ 0 & \text{otherwise} \end{cases} \quad (5.10)$$

Then we define the approximate p th moment $M(p, \rho, n)$ as

$$M(p, \rho, n) = \frac{1}{N(\rho, n)} \sum_{i=1}^n \left(\frac{r_i}{\rho}\right)^p \chi(r_i/\rho) \quad (5.11)$$

The approximate dimension d_a is then given by definition as (cf. (2.6))

$$d_a = d(p, \rho, n) = \frac{pM(p, \rho, n)}{1 - M(p, \rho, n)} \quad (5.12)$$

With these definitions, we derive our error estimate in three major steps. We need to assume that $C(r) \sim r^d$ holds in the strong sense with parameters ρ_0 , a and A (see section 2). In our first step, we obtain the coarse absolute bound

$$\left| E\left((r/\rho)^p : r \leq \rho\right) - M(p) \right| \leq \frac{p}{p+d} \left[\frac{A}{a} - \frac{a}{A} \right] \quad (5.13)$$

As we see below, this is not a difficult bound to obtain. In our second step, we obtain a simple Kolmogorov error bound

$$\text{Prob}\left(\left| M(p, \rho, n) - E\left((r/\rho)^p : r \leq \rho\right) \right| \leq \tau\right) \geq 1 - \varphi \quad (5.14)$$

where φ depends on n , τ , a and A . In (5.14), the symbol \gtrsim means "approximately greater than" in the sense explained below. Finally, we combine (5.13) and (5.14) with (5.12) and (2.6) to obtain the following theorem:

Statistical Relative Error Bound Suppose that we have positive numbers A , a and ρ_0 so that the inequality

$$ar^d \leq C(r) \leq Ar^d \quad (5.15)$$

holds for $0 \leq r \leq \rho_0$. In addition, suppose that $0 < \tau < \frac{1}{10}$, $0 < \varphi$, $0 < \rho \leq \rho_0$ and

$$n \geq n(\rho, \tau, \varphi) = \frac{40(2A^2 + aA)}{9a^3\rho^d\tau^2\varphi} \quad (5.16)$$

hold. Then the inequality

$$\text{Prob}\left(\left|\frac{d-d_a}{d}\right| \leq \varepsilon(\Delta_1, \tau, p, d_a)\right) \gtrsim 1 - \varphi \quad (5.17)$$

holds, where we set

$$\varepsilon(\Delta_1, \tau, p, d_a) = \frac{\Delta_1 p + \tau(p + d_a)}{d_a - (p + d_a)(\Delta_1 + \tau)} \frac{p + d_a}{p} \quad (5.18)$$

and

$$\Delta_1 = \frac{A}{a} - \frac{a}{A} \quad (5.19)$$

More precisely, (5.17) should read

$$\text{Prob}\left(\left|\frac{d-d_a}{d}\right| \leq \varepsilon(\Delta_1, \tau, p, d_a)\right) \geq 1 - \varphi - \frac{80}{9} \frac{\eta}{\rho^{2d} \tau^2 a^2} \quad (5.20)$$

where $\eta > 0$ is a measure of the interdependence of the random variables r_1, r_2, \dots, r_n discussed below; the value of η may be made as small as desired by appropriately lagging the two time series x_1, x_2, \dots, x_n and y_1, y_2, \dots, y_n .

As outlined above, our first step in deriving (5.17) is to verify (5.13). We may use the following simple argument to estimate the limiting moment $M(p)$ with some degree of accuracy. We recall that the moment $E((r/\rho)^p : r \leq \rho)$ is given by the Stieltjes integral (2.4):

$$E((r/\rho)^p : r \leq \rho) = \frac{1}{\rho^p C(\rho)} \int_0^\rho r^p dC(r) \quad (5.21)$$

Then integration by parts leads us to

$$E((r/\rho)^p : r \leq \rho) = 1 - \frac{p}{\rho^p C(\rho)} \int_0^\rho r^{p-1} C(r) dr \quad (5.22)$$

Finally, for $0 < \rho < \rho_0$, we may use (2.7) to conclude that we have

$$1 - \frac{A}{a} \frac{p}{p+d} \leq E((r/\rho)^p : r \leq \rho) \leq 1 - \frac{a}{A} \frac{p}{p+d} \quad (5.23)$$

Thus we see that for $0 < \rho < \rho_0$, both the moment $E((r/\rho)^p : r \leq \rho)$ and its limit $M(p)$ as $\rho \rightarrow 0$ must lie in the interval $[1 - (A/a)(p/(p+d)), 1 - (a/A)(p/(p+d))]$. Consequently, we have the bound (5.13) for the error $|E((r/\rho)^p : r \leq \rho) - M(p)|$. In general, this is a very crude bound; however, this bound is not crude when the values of A and a nearly agree, as in the case of the Henon map discussed in the next section.

Our first step completed, we turn to the second one of deriving (5.14). As noted at the beginning of this section, we study the distances between corresponding points on a pair of time series in the attractor. More specifically, we consider a dynamical system given by an invertible C^1 diffeomorphism $F: \mathbf{R}^N \rightarrow \mathbf{R}^N$ with a chaotic compact attractor that is the closed support of a probability measure μ , invariant and ergodic with respect to F . In addition, we suppose that the measure $\mu \times \mu$ on $\mathbf{R}^N \times \mathbf{R}^N$ is strongly mixing and therefore

ergodic with respect to the map $F \times F$. We let $F' = F \circ F'^{-1}$ and $F^1 = F$. Then by definition, for $\mu \times \mu$ -almost all initial point pairs (x_0, y_0) , the time series of distances

$$r_i = |F^i x_0 - F^i y_0| \quad (5.24)$$

may be used to compute the normalized moment $E\left(\left(\frac{r}{\rho}\right)^p : r \leq \rho\right)$ as the limiting average

$$E\left(\left(\frac{r}{\rho}\right)^p : r \leq \rho\right) = \lim_{n \rightarrow \infty} \frac{1}{N(\rho, n)} \sum_{i=1}^n \left(\frac{r_i}{\rho}\right)^p \chi(r_i/\rho) \quad (5.25)$$

where $\chi(\xi)$ is the characteristic function defined by (5.10) and $N(\rho, n)$ is the number of distances r_i such that $r_i \leq \rho$ and $i \leq n$, defined by (5.9).

For simplicity, we assume that each new value of $\left(\frac{r_i}{\rho}\right)^p \chi(r_i/\rho)$ is an independent estimate of the mean in

$$M_0(p, \rho, n) = \frac{1}{n} \sum_{i=1}^n \left(\frac{r_i}{\rho}\right)^p \chi(r_i/\rho) \quad (5.26)$$

Using our ergodic hypothesis, we note that we may write

$$E\left(\left(\frac{r}{\rho}\right)^p \chi(r/\rho)\right) = \lim_{n \rightarrow \infty} M_0(p, \rho, n) \quad (5.27)$$

As we show next, this expectation is closely related to $E\left(\left(\frac{r}{\rho}\right)^p : r \leq \rho\right)$, the one we seek.

Using our ergodic hypothesis again, we see that we have

$$C(\rho) = \lim_{n \rightarrow \infty} \frac{N(\rho, n)}{n} \quad (5.28)$$

thereby allowing us to take the limit in (5.25) with the result

$$E\left(\left(\frac{r}{\rho}\right)^p : r \leq \rho\right) = \frac{1}{C(\rho)} E\left(\left(\frac{r}{\rho}\right)^p \chi(r/\rho)\right) \quad (5.29)$$

To see that in a fairly general sense we may assume that each new value of $(r_i/\rho)^p \chi(r_i/\rho)$ may be regarded as an independent estimate, we note that the mixing hypothesis implies that the formula

$$\lim_{m \rightarrow \infty} \int \int f(x, y) f(F^m x, F^m y) d\mu(x) d\mu(y) = \left(\int \int f(x, y) d\mu(x) d\mu(y) \right)^2 \quad (5.30)$$

holds for any (integrable and square integrable) function $f(x, y)$. We apply (5.30) to the two choices $f(x, y) = (|x - y|/\rho)^p \chi(|x - y|/\rho)$ and $f(x, y) = \chi(|x - y|/\rho)$ to find a value of m making the difference of the resulting integrals smaller than a preset positive number η for all values of ρ smaller than some ρ_0 . Then we replace F^m with F in the result so that we have

$$\left(\int \int f(x, y) d\mu(x) d\mu(y) \right)^2 - \eta \leq \int \int f(x, y) f(Fx, Fy) d\mu(x) d\mu(y) \leq \left(\int \int f(x, y) d\mu(x) d\mu(y) \right)^2 + \eta \quad (5.31)$$

for our two choices of $f(x, y)$. Then (5.31) expresses the near independence we seek.

The conditional variance $\text{Var}(p, \rho)$ of the random variable $(r/\rho)^p \chi(r/\rho)$, subject to the constraint that $r \leq \rho$, is given by

$$\text{Var}(p, \rho) = E\left((r/\rho)^{2p} \chi(r/\rho)\right) - \left[E\left((r/\rho)^p \chi(r/\rho)\right)\right]^2 \quad (5.32)$$

Then we may use the Kolmogorov Inequality (Feller, 1957) to bound the probability that the approximate mean $M_0(p, \rho, n)$, given by (5.26), differs from the actual value $E\left((r/\rho)^p \chi(r/\rho)\right)$ by a magnitude greater than $\rho^{d+\delta}$, where $\delta > 0$ is to be determined. That is, we have

$$\text{Prob}\left\{|M_0(p, \rho, n) - E\left((r/\rho)^p \chi(r/\rho)\right)| \geq \rho^{d+\delta}\right\} \leq \frac{\text{Var}(p, \rho)}{\rho^{2d+2\delta} n} + \frac{\eta}{\rho^{2d+2\delta}} \quad (5.33)$$

where η is the deviation from independence associated with (5.31) for our two choices $f(x, y) = (|x - y|/\rho)^p \chi(|x - y|/\rho)$ and $f(x, y) = \chi(|x - y|/\rho)$. We may rewrite (5.33) in the approximate form

$$\text{Prob}\left(\left|M_0(p, \rho, n) - E\left((r/\rho)^p \chi(r/\rho)\right)\right| \geq \rho^{d+\delta}\right) \leq \frac{\text{Var}(p, \rho)}{\rho^{2d+2\delta} n} \quad (5.34)$$

In the same way, we note that we have, by definition,

$$C(\rho) = E(\chi(r/\rho)) \quad (5.35)$$

Then we see that, because

$$\chi(r/\rho)^2 = \chi(r/\rho) \quad (5.36)$$

holds, we must have

$$C(\rho) - C(\rho)^2 = \text{Var}(\chi(r/\rho)) \quad (5.37)$$

Then we may use the Kolmogorov Inequality again to obtain, approximately

$$\text{Prob}\left(\left|N(\rho, n)/n - C(\rho)\right| \geq \rho^{d+\delta}\right) \leq \frac{C(\rho) - C(\rho)^2}{\rho^{2d+2\delta} n} \quad (5.38)$$

We may combine (5.33) and (5.38) to obtain the estimate

$$\begin{aligned} & \text{Prob}\left(\left|M_0(p, \rho, n) - E\left((r/\rho)^p \chi(r/\rho)\right)\right| < \rho^{d+\delta} \quad \text{and} \quad \left|N(\rho, n)/n - C(\rho)\right| < \rho^{d+\delta}\right) \\ & \geq 1 - \left(\frac{\text{Var}(p, \rho)}{\rho^{2d+2\delta} n} + \frac{C(\rho) - C(\rho)^2}{\rho^{2d+2\delta} n}\right) \end{aligned} \quad (5.39)$$

The rest of this argument justifying (5.14) is routine but messy and so we transfer it to Appendix A. The conclusion of our argument shows that whenever the conditions $0 \leq \tau \leq \frac{1}{10}$ and (5.16), which is $n \geq 40(2A^2 + Aa)/(9\phi\rho^d a^3 \tau^2)$, hold, we have (5.14), which is

$$\text{Prob}\left(\left|M(p, \rho, n) - E\left((r/\rho)^p : r \leq \rho\right)\right| \leq \tau\right) \geq 1 - \phi \quad (5.40)$$

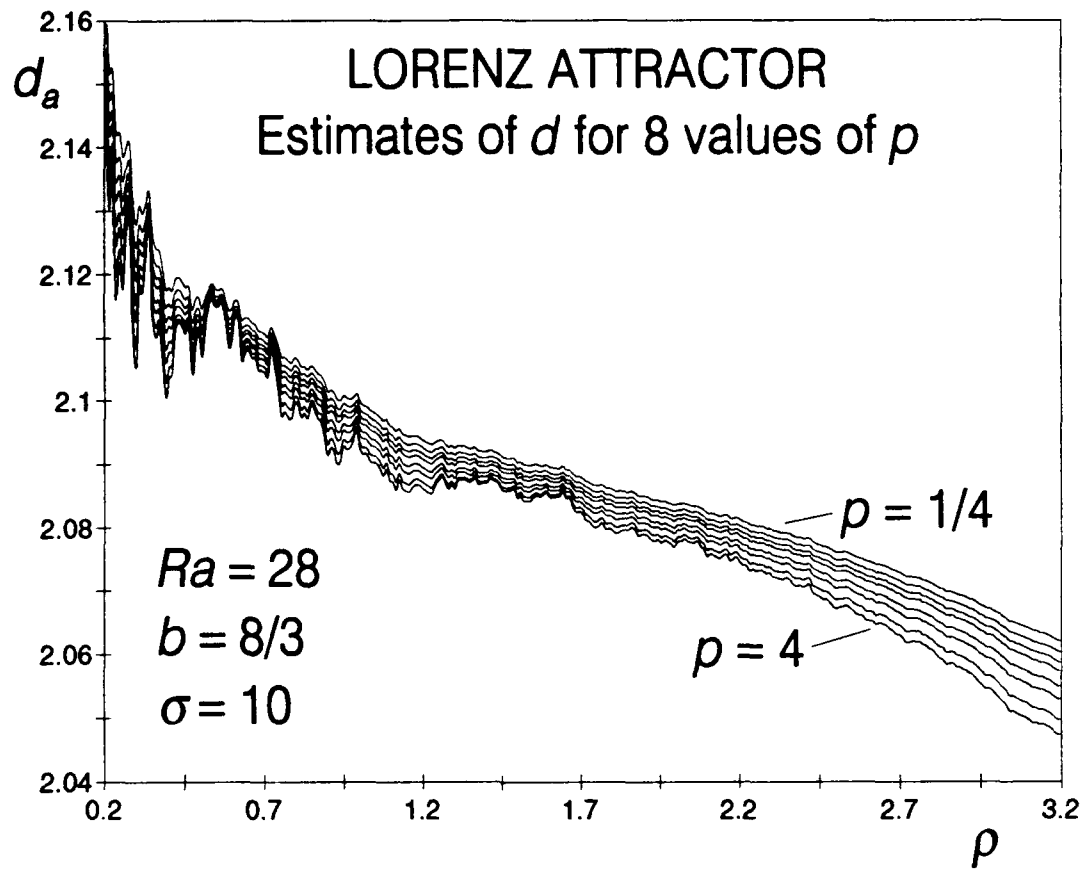
Finally, we must derive the bound (5.17) from (5.13) and (5.14). Once this derivation is complete, so is the justification of the Statistical Relative Error Bound. It is fairly clear what must be done to derive (5.17), but unfortunately the details are again messy, so we place them in Appendix B.

6. Estimating the Correlation Dimension for the Lorenz and Henon Attractors

A fundamental problem in interpreting an estimate of the correlation dimension such as that given in Figure 1 for the Lorenz attractor is determining the reliability of this estimate. With the integral method for estimating d , we may address this problem using two distinct methods. First, by evaluating the approximants d_a of d given by (5.12) for many values of p and ρ , we may identify those values of ρ for which these approximants cluster somewhat as the value of p varies. Second, we may use the statistical techniques introduced in section 5 to find the probability that the numerically estimated value of d_a lies with probability at least $1-\phi$ within a calculable error bound $\epsilon(\Delta_1, \tau, p, d_a)$ (5.18) of the actual value d .

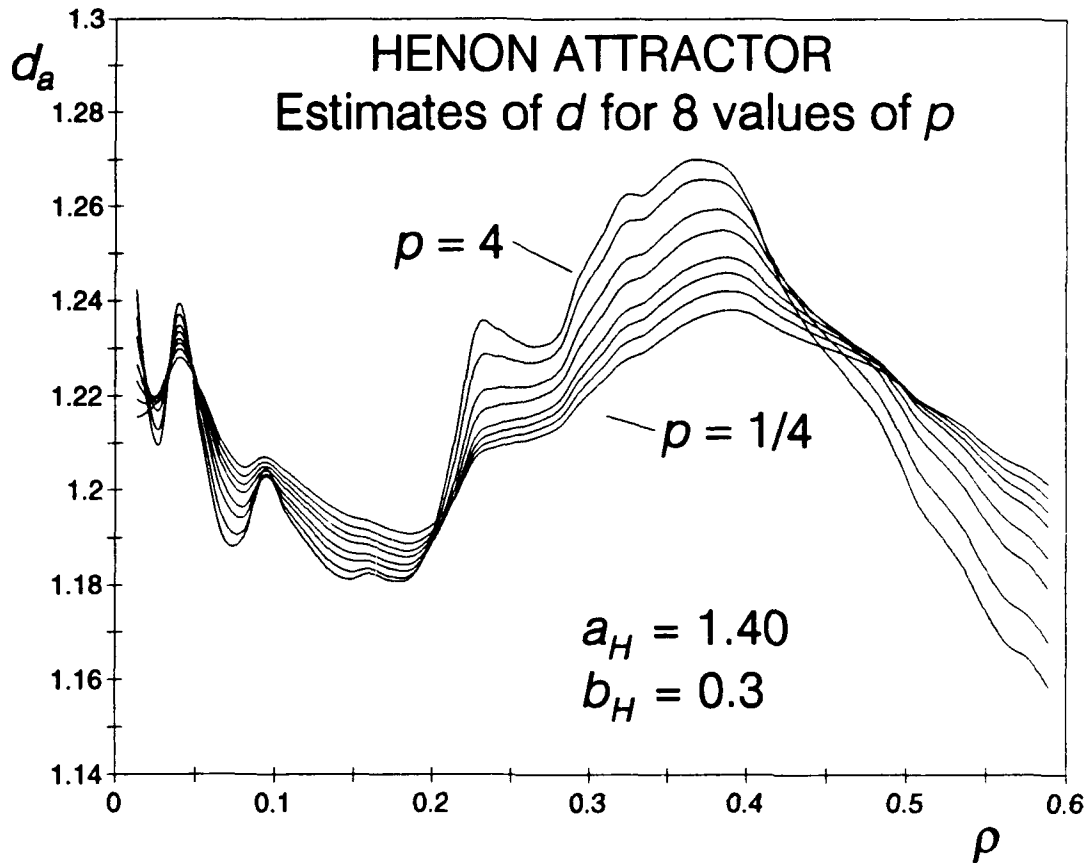
We may illustrate the first method by estimating the value of the correlation dimension d for the standard Lorenz and Henon attractors (with parameter values $Ra = 28$, $\sigma = 10$, $b = \frac{8}{3}$ as in Lorenz, 1963; and $a_H = 1.40$, $b_H = 0.3$ as in Henon, 1976). For each attractor, we use the values $p = \frac{1}{4}, \frac{1}{2}, \frac{3}{4}, 1, \frac{3}{2}, 2, 3, 4$ to estimate the limiting moment $M(p)$ using the approximate moment $M(p, \rho, n)$ (5.11) from a sequence $r_1, r_2, r_3, \dots, r_n$ of distances numerically generated in the usual way. Here we use the classical method for generating distances r_1, r_2, r_3, \dots in the order they are calculated from a single generic trajectory; as noted in section 5, this is essentially equivalent to the method introduced in that section for generating the distances from a generic pair of trajectories.

In Figure 3, we plot the curves $d = d_a = d(p, \rho, n)$ given by (5.12) for varying values of ρ for the Lorenz attractor (Figure 3a; in which the number k of transient-free time series points is 20,000) and the Henon attractor (Figure 3b; $k = 6000$); here the number of distances $n = k(k-1)/2$ is given by (5.4). As we note below, only a fraction of these distances contribute to the figures. Using any one of these curves, we would look classically for a scaling region in which the curve is relatively constant, and we would declare this constant value to be our estimate for the correlation dimension. As is fairly clear, such a flat segment might be found between approximately $\rho = 1.2$ and $\rho = 1.7$



(a)

Figure 3



(b)

Figure 3. Eight estimates $d_a = d(p, \rho, n)$ (5.12) of the correlation dimension d for the standard Lorenz ($Ra = 28$, $\sigma = 10$, $b = 8/3$) (a) and Henon ($a_H = 1.40$, $b_H = 0.3$) (b) attractors using $p = \frac{1}{4}, \frac{1}{2}, \frac{3}{4}, 1, \frac{3}{2}, 2, 3, 4$; in both cases, the curves vary monotonically from the one for $p = \frac{1}{4}$ to the one for $p = 4$. For the Lorenz attractor, 20,000 transient-free time series points and 10,000 bins are used, while for the Henon attractor 6000 points and 200 bins are used, although only a fraction of these contribute to the given ranges in ρ .

for the Lorenz attractor (Figure 3a), but it is impossible to find for the Henon attractor (Figure 3b). The relatively flat segment for the Lorenz attractor is also a region in which the dimension curves cluster, giving values for d between 2.08 and 2.09; these values are close to those given by the slope estimates for small values of ρ in Figure 1a as well as to those in the literature (e.g., Grassberger and Procaccia, 1983a, b and Nese *et al.*, 1987 report $d = 2.05 \pm 0.01$; Simm *et al.*, 1987 find $d = 2.16 \pm 0.3$). In contrast, the estimates of d for the Henon attractor do not cluster consistently over any range of ρ , leading to a large uncertainty in the estimate for d . The best we can say is that d apparently lies between 1.17 and 1.27 for ρ between 0 and 0.5 or between 1.21 and 1.27 for ρ between 0.25 and 0.45; these values are nevertheless in the range reported in the literature (e.g., Grassberger and Procaccia, 1983a, b cite 1.21 ± 0.01 when the full map is used, but 1.25 ± 0.02 when the time series from a single variable is used; Abraham *et al.*, 1986 find 1.24 ± 0.02 when 10,000 points are used; Simm *et al.*, 1987 report 1.25 ± 0.1 when 8192 points are used; Arneodo *et al.*, 1987 obtain 1.199 ± 0.003 when 10^8 points are used with ρ as small as 2^{-12} ; and Grassberger, 1988 finds 1.2 ± 0.05 when 4×10^6 points are used with ρ as small as 2^{-22}). Nevertheless, Theiler (1988) notes that the Henon attractor is probably nonlacunar, which in our context implies that $a = A$ (e.g., Grassberger, 1988), and therefore that the limiting moment $M(p)$ exists, so that our integral method results probably can be trusted.

By way of caution, we recall that, as remarked at the beginning of section 5, conventional error estimates lead to predicted errors so unrealistically small that at least one of the following three possibilities must hold in order to invalidate these estimates:

- i) The number n is not large enough to justify an appeal to the Central Limit Theorem,
- ii) The observations are not sufficiently independent, or
- iii) The values of r used are not sufficiently small for $E\left(\left(\frac{r}{\rho}\right)^p : r \leq \rho\right)$ and $M(p)$ to be interchangeable.

It seems to us that it is the third of these that is the likely culprit. Thus, as in section 5, we turn from the conventional approach to one yielding coarser but more reliable bounds, using our hypothesis that $C(r) \sim r^d$ holds in the strong sense to diminish some of the uncertainty introduced by possibility iii) above.

To apply this second approach, we need to associate the probability $1 - \varphi$ with the number $n(\rho, \tau, \varphi)$ of independent distances used to estimate d in the empirical scaling region of ρ . As noted above, this scaling region is given classically by $0 < \rho_{\min} < \rho < \rho_0$, in which ρ_{\min} is the smallest distance for which the dimension curves are relatively level and ρ_0 is the largest. This is also a reasonable way to choose the scaling region in our case. To choose appropriate values of ρ_0 , we first note that as the value of ρ increases, the function $M(p, \rho, n)$ approaches 0 for any value of p and n . Thus it immediately follows that the function $pM(p, \rho, n)/(1 - M(p, \rho, n))$ in (5.12) approaches the value of 0 for large values of ρ . Consequently, we expect the beginning of a plunge in the graph of $pM(p, \rho, n)/(1 - M(p, \rho, n))$ to signal the transition beyond the scaling region of ρ . Thus, we choose the largest value ρ_0 of ρ to be the one that marks the beginning of the steady decrease to 0 in the graphs of $pM(p, \rho, n)/(1 - M(p, \rho, n))$ such as those in Figures 3a and 3b. Next we choose a value for $\rho_{\min} < \rho_0$ that is large enough to exclude the noisy, undersampled region for small values of ρ .

Once we have determined the empirical scaling region, we may specify the other parameters needed to estimate the relative error bound for d . A range of trial dimensions d_τ that approximate d_a is given by the variation within this scaling region of d_a with p . As discussed further below, the values of a and A are given by the minimum and maximum values of the ratio $C(\rho)/\rho^{d_\tau}$ within the scaling region. By definition, we have $n(\rho, \varphi, \tau) \sim nC(\rho_0)$. Thus, after reexpressing (5.16) as

$$\varphi\tau^2 \sim \frac{40(2A^2 + aA)}{9a^3\rho_0^{d_\tau}nC(\rho_0)} \quad (6.1)$$

we are able to find acceptable values for φ and τ . If $\rho_0 \leq 1$, then we choose the value of d_τ in (6.1) to be the upper bound of the range for d_τ , while if $\rho_0 > 1$, then we choose the lower bound. We may now use (5.18) to obtain an initial estimate for the relative error bound $\varepsilon(\Delta_1, \tau, p, d_a)$ for d with the associated probability $1-\varphi$ and moment error tolerance τ . This value, however, is not the smallest one available because $\varepsilon(\Delta_1, \tau, p, d_a)$ depends on both p and d_a , which are parameters that may be regarded as varying independently within suitable bounds.

To find this minimum value of the relative error bound, we thus regard as fixed the values of τ and Δ_1 , which is given in (5.19) by the known values of a and A . Then we hold d_a constant and minimize the value of $\varepsilon(\Delta_1, \tau, p, d_a)$ with respect to p . Using the symbolic manipulator Derive, we find that this minimum value is given by

$$\varepsilon_{\min}(\Delta_1, \tau, d_a) = -\frac{[\sqrt{\tau(1-\Delta_1)} + \sqrt{\Delta_1 + \tau}][\sqrt{(\Delta_1 + \tau)(1-\Delta_1)} - \sqrt{\tau(\Delta_1 - 1)}]}{[\sqrt{(1-\Delta_1)} - \sqrt{\tau(\Delta_1 + \tau)}][\sqrt{\tau(\Delta_1 + \tau)(1-\Delta_1)} + \Delta_1 - 1]} \quad (6.2)$$

We note that this minimum value is actually independent of d_a and, because it is attained for every value of d_a , it must be the global minimum $\varepsilon_{\min}(\Delta_1, \tau) = \varepsilon_{\min}(\Delta_1, \tau, d_a)$ that we seek. The value p_{\min} of p yielding (6.2) is given by

$$p_{\min} = \frac{d_a}{\tau+1} \left[\sqrt{\frac{\tau(1-\Delta_1)}{\Delta_1 + \tau}} - \tau \right] \quad \text{for } \Delta_1 < 1 \quad (6.3)$$

There are two limiting cases of interest. First, for the case $\tau = 0$ of perfect estimates for $E((r/\rho)^p : r \leq \rho)$, we cannot find a relative error bound smaller than

$$\varepsilon_{\min}(\Delta_1, 0) = \frac{\Delta_1}{1-\Delta_1} \quad (6.4)$$

for any τ . We call this the *geometric part* of the error because it is intrinsic to the geometry of $C(\rho)$, unlike the error τ that is due to noise introduced by undersampling at small values of ρ . In this perfect case, p_{\min} must vanish, which is forbidden because $p > 0$ is required in (5.18). However, we may interpret $p_{\min} = 0$ as meaning that, no matter what value of p we

use to estimate a relative error bound for d , we could find a better estimate using a still smaller value of p . Second, for the case $\Delta_1 = 0$, we obtain the limiting relative error bound

$$\varepsilon_{\min}(0, \tau) = \frac{4\tau}{(1-\tau)^2} \quad (6.5)$$

with corresponding p_{\min} given by

$$p_{\min} = d_a \frac{1-\tau}{1+\tau} \quad (6.6)$$

We call $\varepsilon_{\min}(0, \tau)$ the *statistical part* of the error because it arises from random errors in measurement. Below we calculate (6.2), (6.4) and (6.5) to see how close our error bound $\varepsilon_{\min}(\Delta_1, \tau)$ is to the limiting error bounds $\varepsilon_{\min}(\Delta_1, 0)$ and $\varepsilon_{\min}(0, \tau)$.

For the Lorenz attractor, we inspect Figure 3a to obtain the estimates $\rho_0 \sim 1.7$ and $\rho_{\min} \sim 1.2$ for the scaling region, while for the Henon attractor we obtain $\rho_0 \sim 0.45$ and $\rho_{\min} \sim 0.25$. The value of $n(\rho, \varphi, \tau) \sim nC(\rho_0)$ for the Lorenz attractor is $n(\rho, \varphi, \tau) \sim 1 \times 10^6$, while for the Henon attractor it is $n(\rho, \varphi, \tau) \sim 5 \times 10^6$. To find the values of a and A , we calculate the ratio $C(\rho)/\rho^{d_\tau}$ for several trial dimensions d_τ that are suggested by the plots of d_a versus ρ in Figure 3. It is clear from these figures that $2.08 \leq d_\tau \leq 2.10$ for the Lorenz attractor, while $1.21 \leq d_\tau \leq 1.27$ for the Henon attractor. Within the empirical scaling region $\rho_{\min} < \rho < \rho_0$, the indicated value for a is the minimum value of the ratio $C(\rho)/\rho^{d_\tau}$, while A is the maximum value, as given by (2.7). Of course, by definition a and A are the minimum and maximum values of $C(\rho)/\rho^{d_\tau}$ over the *entire* range $0 < \rho < \rho_0$. But, owing to the unavoidable undersampling of the attractor given by our finite dataset, we must attempt to estimate the values of a and A from the behavior of $C(\rho)/\rho^{d_\tau}$ within only the chosen scaling region. Finally, we note that, if Theiler (1988) is correct, then the actual values of a and A should be equal for the Henon attractor (Grassberger, 1988). However, we will not assume them to be equal in our error estimates below, and so use the following numerical values for a and A giving $\Delta_1 \neq 0$. For the Lorenz attractor, we find $a \sim 0.00215$ and $A \sim 0.00217$ (not shown), and for the Henon attractor, $a \sim 0.716$ and $A \sim 0.778$ (Figure 4).

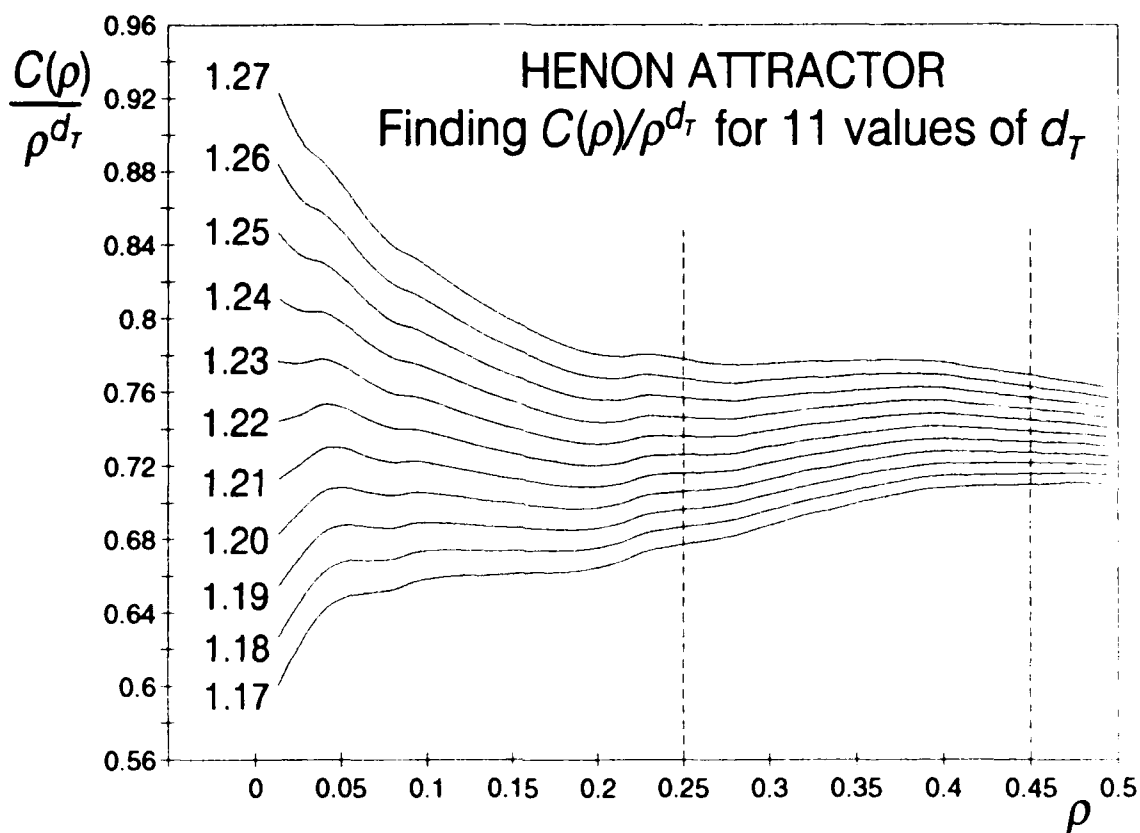


Figure 4. Estimates of the ratio $C(\rho)/\rho^{d_T}$ for 11 trial values d_T of the correlation dimension d for the Henon attractor ($a_H = 1.40$, $b_H = 0.3$). The maximum value of this ratio in the empirical scaling region $\rho_{\min} < \rho < \rho_0$, given by $\rho_{\min} = 0.25$ and $\rho_0 = 0.45$ and denoted by the dashed lines, provides an estimate for A , while the minimum value gives a . Here 6000 points and 200 bins are used, although only a fraction of these contribute to the distance interval used.

Our next task is to estimate the product $\varphi\tau^2$ using (6.1), under the *assumption* that we actually have $n(\rho, \tau, \varphi)$ independent evaluations of the distances. With the above values of $a, A, d_\tau, \rho_{\min}$, and $n(\rho, \tau, \varphi)$, we find that $\varphi\tau^2 \sim 2 \times 10^{-3}$ for the Lorenz attractor, while $\varphi\tau^2 \sim 1 \times 10^{-5}$ for the Henon attractor. Estimates using (6.2) show that acceptable relative error bounds of no more than 15% to 20% are only achieved if $\tau \leq 0.03$. With $\varphi \leq 0.2$ to give a probability of at least 80% that we have a good estimate for d , we conclude that we would need to have $\varphi\tau^2 \leq 2 \times 10^{-4}$. Although we used 20,000 points giving approximately 2×10^8 distances in our estimates for the Lorenz attractor, we have only 10% of the distances we need in the scaling region $\rho_{\min} < \rho < \rho_0$ for us to find acceptable relative error bounds for d ; such a calculation would require 200,000 time series points, which is 10 times that normally considered in an estimate of d (e.g., Grassberger and Procaccia, 1983a, b). In contrast, the 6000 points we used for the Henon attractor give enough distances in the scaling region to allow us to produce acceptable relative error bounds for d .

We now are ready to estimate the relative error bounds $\varepsilon(\Delta_1, \tau, \rho, d_a)$ (5.18), $\varepsilon_{\min}(\Delta_1, \tau)$ (6.2), $\varepsilon_{\min}(\Delta_1, 0)$ (6.4), and $\varepsilon_{\min}(0, \tau)$ (6.5) for the Henon attractor. Two combinations of φ and τ satisfying the above condition on $\varphi\tau^2 \sim 1 \times 10^{-5}$ are used: $\tau = 0.02$, $\varphi = 0.025$ and $\tau = 0.01$, $\varphi = 0.1$. These results are reported in Table 1 and illustrated in Figures 4 and 5. Inspection of Table 1 reveals that the smallest error occurs for $d_\tau = 1.26$, and inspection of Figure 4 shows that the ratio $C(\rho)/\rho^{d_\tau}$ varies the least in the empirical scaling region for this value of d_τ . The geometric part $\varepsilon_{\min}(\Delta_1, 0)$ of the error implies an estimate of at least $d_\tau = 1.25 \pm 0.02$, while the statistical part implies $d_\tau = 1.25 \pm 0.1$ with probability 97.5% or $d_\tau = 1.25 \pm 0.05$ with probability 90%. In contrast, the complete relative error bound $\varepsilon_{\min}(\Delta_1, \tau)$ leads to the estimates $d_\tau = 1.25 \pm 0.15$ with probability 97.5% and $d_\tau = 1.25 \pm 0.1$ with probability 90%. Incidentally, the second complete estimate agrees with the more *ad hoc* one of Simm *et al.* (1987) and the geometric part agrees with the *ad hoc* one of Grassberger and Procaccia (1983a, b).

Table 1. Estimates for the Henon attractor, expressed as a percent of d , of the relative errors $\epsilon(\Delta_1, \tau, p, d_a)$ when $p = 1$ (5.18), $\epsilon_{\min}(\Delta_1, \tau)$ (6.2) when $p = p_{\min}$ (6.3), the geometric part $\epsilon_{\min}(\Delta_1, 0)$ (6.4), and the statistical part $\epsilon_{\min}(0, \tau)$ (6.5) that are associated with a range of trial values d_T for the correlation dimension d . The scaling interval in ρ , given by Figure 3b, is [0.25, 0.45]. Two choices of φ and τ satisfying the condition (6.1) on $\varphi\tau^2$ are considered: $\tau = 0.02$, $\varphi = 0.025$ and $\tau = 0.01$, $\varphi = 0.1$. The resulting estimates are $d_T = 1.25 \pm 0.15$ with probability 97.5% and $d_T = 1.25 \pm 0.1$ with probability 90%. The minimum geometric part of the relative error is 1.9%, while the statistical part is 8.3% when $\tau = 0.02$ and 4.1% when $\tau = 0.01$, with $p_{\min} \sim 1.2$ in either case.

Parameters for scaling interval										
d_T	a	A	Δ_1	$\epsilon_{\min}(\Delta_1, 0)$ (in % of d)	$\tau = 0.02, \varphi = 0.025$			$\tau = 0.01, \varphi = 0.1$		
					$\epsilon(\Delta_1, \tau, p, d_a)$ (in % of d) for $p = 1$	p_{\min}	$\epsilon_{\min}(\Delta_1, \tau)$ (in % of d) for $p = p_{\min}$	$\epsilon(\Delta_1, \tau, p, d_a)$ (in % of d) for $p = 1$	p_{\min}	$\epsilon_{\min}(\Delta_1, \tau)$ (in % of d) for $p = p_{\min}$
1.21	0.7157	0.7344	0.0516	5.4	20.1	0.587	18.7	15.2	0.458	13.3
1.22	0.7257	0.7411	0.0420	4.4	17.7	0.641	16.9	12.9	0.506	11.6
1.23	0.7357	0.7480	0.0332	3.4	15.6	0.703	15.1	10.9	0.564	10.1
1.24	0.7455	0.7551	0.0256	2.6	13.9	0.771	13.6	9.3	0.630	8.8
1.25	0.7551	0.7623	0.0190	1.9	12.4	0.845	12.3	7.9	0.708	7.7
1.26	0.7625	0.7696	0.0185	1.9	12.3	0.857	12.2	7.8	0.719	7.6
1.27	0.7685	0.7775	0.0233	2.4	13.3	0.812	13.2	8.7	0.669	8.4

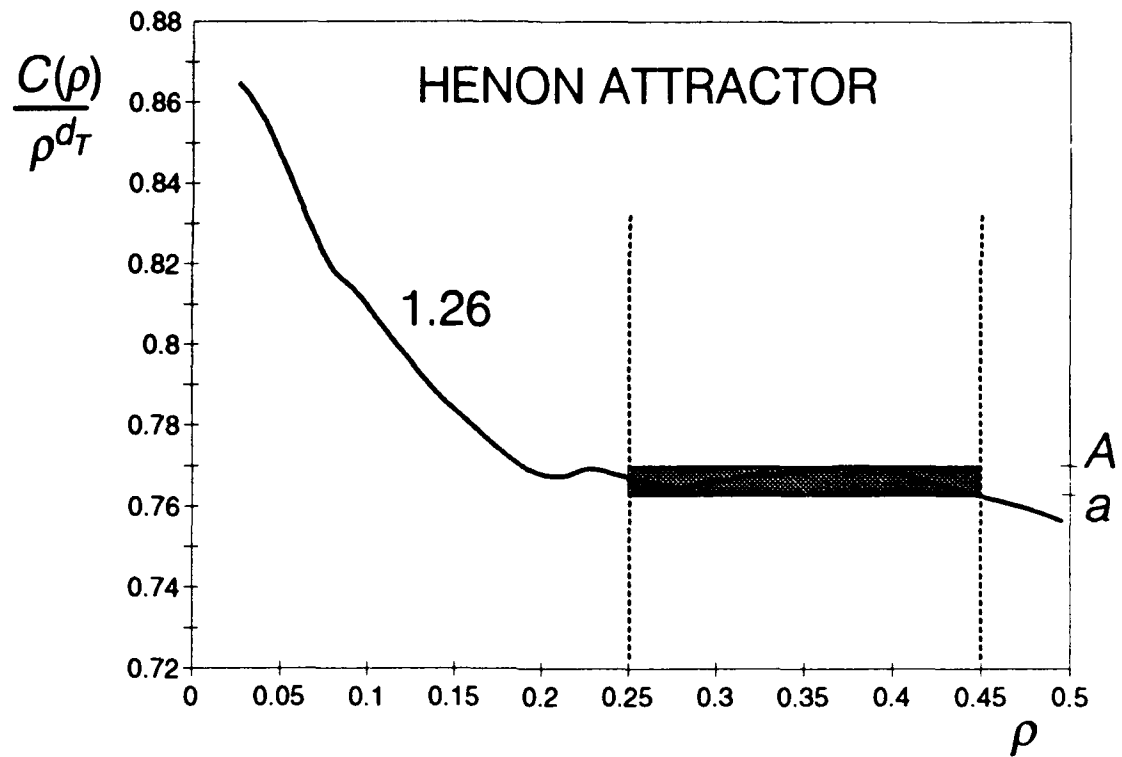


Figure 5. Illustration of how the optimal value d_T for the correlation dimension d can be found by minimizing the variation of $C(\rho)/\rho^{d_T}$ for the Henon attractor ($a_H = 1.40$, $b_H = 0.3$). The curve $d_T = 1.26$ corresponds to the case in Table 1 that minimizes the height $A - a$ of the shaded rectangle in the figure. The empirical scaling region $\rho_{\min} < \rho < \rho_0$ is indicated by the dotted lines.

Although our estimates are very coarse, they are objectively determined and identify the most likely value for the correlation dimension d that can be obtained from a transient-free time series. Inspection of (6.2) and Table 1 reveals that the values for p_{\min} are not needed to identify the optimum value of d . The error bounds are closest when the value of Δ_1 is smallest, and from its definition (5.19), we see that this occurs when the difference $A - a$ is smallest. Thus, we need only plot the ratio $C(\rho)/\rho^{d_\tau}$ as a function of ρ for various candidate values d_τ , and then seek the value producing the smallest difference $A - a$. These candidate values are given by the approximants d_a that are calculated using the moment $M(p, \rho, n)$ via (5.12).

The procedure of minimizing $A - a$ is illustrated in Figure 5, in which we reproduce one of the curves in Figure 4. As indicated by the more thorough analysis in Table 1, the difference $A - a$ is smallest for the case $d_\tau = 1.26$ for the Henon attractor. Although finding the values of a and A that minimize $A - a$ leads to the geometric part $\epsilon_{\min}(\Delta_1, 0)$ of the relative error bound for d , it does not reveal anything about the statistical, and major, part resulting from the moment error tolerance τ (see Table 1). Nor does it reveal the magnitude $\epsilon(\Delta_1, \tau, p, d_a)$ or $\epsilon_{\min}(\Delta_1, \tau)$ of this error. We therefore recommend that a full analysis of the relative error bounds be performed to see if they are small enough to allow acceptance, with reasonably high probability, of the estimated values for d .

7. Hentschel-Procaccia Dimensions

Hentschel and Procaccia (1983) introduce a scale of dimensions generalizing the Grassberger-Procaccia (1983a, b) correlation dimension d . The same device that we have used in section 2 may be used to improve the numerical estimates of the Hentschel and Procaccia dimensions as well. However, we first need to establish some background and notation before applying that device.

We assume that we have a C^1 diffeomorphism $F: \mathbf{R}^N \rightarrow \mathbf{R}^N$ and a probability measure μ such that $F \times \dots \times F: \mathbf{R}^N \times \dots \times \mathbf{R}^N \rightarrow \mathbf{R}^N \times \dots \times \mathbf{R}^N$ is ergodic with respect to $\mu \times \dots \times \mu$. Then for $q=1, 2, 3, \dots$ we may define the corresponding Hentschel-Proccaccia dimension $D(q)$ by setting first

$$C_q(r) = \int \mu(B(x, r))^q d\mu(x) \quad (7.1)$$

where $B(x, r)$ is the ball of radius r and center x ,

$$B(x, r) = \{y \mid |x - y| \leq r\} \quad (7.2)$$

Then we define D_q with the limit equation

$$D_q = \frac{1}{q} \lim_{r \rightarrow 0} \frac{\ln C_q(r)}{\ln r} \quad (7.3)$$

provided this limit exists. We recall from (2.2) that the correlation dimension $d = D_1$.

We note that we have

$$\mu(B(x, r)) = \int \chi(|x - y|/r) d\mu(y) \quad (7.4)$$

where $\chi(\xi)$ is given by (5.10), so that

$$C_q(r) = \int \dots \int \chi(|x - y_1|/r) \dots \chi(|x - y_q|/r) d\mu(y_1) \dots d\mu(y_q) d\mu(x) \quad (7.5)$$

holds. We define a function $r_q(x, y_1, \dots, y_q)$ by setting

$$r_q(x, y_1, \dots, y_q) = \min\{|x - y_1|, \dots, |x - y_q|\} \quad (7.6)$$

Then we have

$$C_q(r) = \int \dots \int \chi(r_q(x, y_1, \dots, y_q)/r) d\mu(y_1) \dots d\mu(y_q) d\mu(x) \quad (7.7)$$

Now we introduce a family of limiting moments $M_q(p)$ by setting

$$M_q(p) = \lim_{\rho \rightarrow 0} E\left(\left(r_q/\rho\right)^p : r_q \leq \rho\right) \quad (7.8)$$

provided that the limit exists. We note that we have $M_1(p) = M(p)$.

We use (7.7) to conclude that $C_q(\rho)$ is the probability that $r_q \leq \rho$ so that we have

$$E\left(\left(r_q/\rho\right)^p : r_q \leq \rho\right) = \frac{1}{\rho^p C_q(\rho)} \int_0^\rho s^p dC_q(s) \quad (7.9)$$

Integrating by parts, we obtain, for $p+d > 1$,

$$\int_0^\rho s^p dC_q(s) = \rho^p C_q(\rho) - p \int_0^\rho s^{p-1} C_q(s) ds \quad (7.10)$$

and arguing as in section 2, we obtain

$$\lim_{\rho \rightarrow 0} \frac{\rho^p C_q(\rho)}{\int_0^\rho s^{p-1} C_q(s) ds} = p + qD_q \quad (7.11)$$

provided that the limit exists.

We use (7.9)-(7.11) to arrive at the result

$$qD_q = \frac{pM_q(p)}{1 - M_q(p)} \quad (7.12)$$

provided only that both D_q and $M_q(p)$ exist. In addition, we may extend the Takens (1985) formulas (4.2) and (4.3) to

$$\lim_{\rho \rightarrow 0} E\left([\ln(r_q/\rho)] : r_q \leq \rho\right) = -\frac{1}{qD_q} \quad (7.13)$$

and

$$\lim_{\rho \rightarrow 0} E\left([\ln(r_q/\rho)]^2 : r_q \leq \rho\right) = \frac{2}{q^2 D_q^2} \quad (7.14)$$

Finally we extend (4.1) to

$$M_q(p, \gamma) = \lim_{\rho \rightarrow 0} E\left(\left(r_q/\rho\right)^p [\ln(r_q/\rho)]^\gamma : r_q \leq \rho\right) = (-1)^\gamma \frac{qD_q \gamma!}{[p + qD_q]^{\gamma+1}} \quad (7.15)$$

where $M_1(p, \gamma) = M(p, \gamma)$.

8. Concluding Remarks

In this article we present a new method for estimating the value of the Grassberger and Procaccia (1983a, b) correlation dimension d . This method connects the dimension at the origin of a continuous probability distribution $C(r)$ on $[0, \infty)$ with its limiting moment $M(p)$ at the origin. More specifically, we define the dimension of $C(r)$ at the origin to have the value of d if the relation $C(r) \sim r^d$ holds in the weak sense (defined in section 2) as r approaches zero. If the dimension has a finite value d , then the expected value of the random variable $(r/\rho)^p$, relative to the condition $r \leq \rho$, has limit $M(p)$, given by (2.5), as r approaches zero. The connection between the limiting moment and the dimension d is given by the simple formula (2.6),

$$d = \frac{pM(p)}{1 - M(p)} \quad (8.1)$$

The classical algorithm for estimating the dimension identifies it with the limit given by

$$d = \lim_{r \rightarrow 0} \frac{d \ln C(r)}{d \ln r} = \lim_{r \rightarrow 0} \frac{r}{C(r)} \frac{dC(r)}{dr} \quad (8.2)$$

Therefore, this algorithm requires the function $C(r)$ to be differentiable, and then the slopes of the function $y = \ln C(\exp x)$ approach d as x approaches $-\infty$ (where $x = \ln r$). However, because numerical differentiation is very sensitive to errors (see Figure 1a), various kinds of mean slopes are used instead to generate a numerically stable algorithm.

The method we introduce here, leading to (8.1), uses the hypothesis that $C(r)$ is continuous. Instead of differentiating, we integrate to define the function $I(\rho)$ given by

$$I(\rho) = \int_0^\rho C(r) dr \quad (8.3)$$

We easily see that this new function satisfies the relation $I(\rho) \sim \rho^{d+1}$ so that

$$d+1 = \lim_{\rho \rightarrow 0} \frac{\rho C(\rho)}{I(\rho)} \quad (8.4)$$

holds, provided the limit exists. This formula is similar to one suggested by Theiler (1988, 1990).

By using (8.4) in place of (8.2), we eliminate the need for numerical slope-finding routines, replacing them with the more stable numerical integration routines required for tabulating the new function $I(\rho)$ (see, for example, Figure 1b). In addition, by using algorithms based on (8.4) instead of (8.2), we also extend the applicability of the dimension-finding algorithms to the important case for which $C(r)$ is not differentiable. However, to improve directly the accuracy of an algorithm based on (8.4), we require more accurate numerical integration of the nondifferentiable monotone continuous function $C(r)$. Because an algorithm other than Riemann sums is not available, we use instead a Stieltjes integration by parts to transform (8.4) into (8.1), which requires only evaluation of certain means, thereby bypassing errors introduced by using inadequate numerical integration routines. By evaluating these means, we eliminate the need to order by magnitude the set of distances, as is often done in the classical slope procedure (Albano *et al.*, 1988) but that is computationally very expensive for datasets of the large size required to produce usable error bounds (see section 6). Finally, integral methods, based on (8.2) or (8.1), make it unnecessary to find the function $C(r)$ before finding the dimension d .

A further advantage of integral methods over slope methods is the apparently superior rate of convergence of the former (Theiler, 1988). In any numerical or empirical approximation of the probability distribution $C(r)$, the smaller distances are noise-dominated in comparison with the larger. What results is a function $C_c(r)$ approximating $C(r)$ well for large values of r and poorly for small values of r . As Ben-Mizrachi *et al.* (1984), Simm *et al.* (1987), and Theiler (1986, 1991) note, $C_c(r)$ scales with the dimension d for large values of r , but with the much larger embedding dimension $c \sim 2d+1$ for small

values of r when the correlation integral estimate is contaminated by noise. We model this situation by considering the special nonlacunar case of an actual distribution $C(r) = r^d$ that is approximated by a continuous distribution $C_e(r)$ given by

$$C_e(r) = \begin{cases} \delta^{d-c} r^c & \text{for } 0 \leq r \leq \delta \\ r^d & \text{for } \delta \leq r \leq \rho \end{cases} \quad (8.5)$$

in which δ is a positive number. Thus we regard those values of r lying below δ as belonging to the noise-dominated region and those lying above δ as belonging to the well-sampled region, with the transition from one region to the other taking place abruptly at $r = \delta$. Then we compare the slope method with the integral method by using the same working interval $[\delta_1, \rho]$, with $0 < \delta_1 < \delta < \rho < 1$, to fit a line in the $\ln C(r) - \ln r$ plane for the slope method and to integrate $C_e(r)$ for the integral method. Thus the first procedure produces the mean slope over the interval $[\delta_1, \rho]$ and the second produces an approximation of $I(\rho)$. From each of these results, we derive the corresponding estimate of d . Upon comparing these two estimates as the proportion $(\delta - \delta_1)/\rho$ of the noise-dominated region decreases to zero through positive values, we find analytically in section 3 that the integral estimate approaches the dimension d much more rapidly than does the slope estimate. In addition, we find numerically an even more dramatic improvement in the rate of convergence (see Figures 2b, c), strongly suggesting that the integral method is far less sensitive to contamination by errors at small values of r than is the slope method. Of course, considerable work remains to be done in this direction: first, to compare these two methods in paradigmatic cases analogous to those given by (8.5), but with a gradual transition from noise-contaminated to well-sampled regions, and, second, to compare the two in the case of a similar blend of more general, especially lacunar, distributions (e.g., Theiler, 1988).

Furthermore, in section 7 we extend the integral method to apply to the case of the Hentschel-Procaccia generalized dimensions of integral index (Hentschel and Procaccia, 1983), and in section 4 we also recover the formulas of Takens (1985).

Besides the apparently more rapid convergence of the integral method over the slope method, a second advantage lies in its formulation in terms of expectations and probabilities: This formulation enables us to use the simple Kolmogorov Inequality to bound, in an *a priori* manner, the probability that our estimate of the dimension differs from the actual dimension by more than a prescribed amount. In this article we begin this process by arriving at somewhat coarse error bounds, and identifying four obstacles to obtaining more refined and satisfactory versions of these. First, our results depend upon the hypothesis that the relation $C(r) \sim r^d$ holds in the strong sense that is defined in section 2; however, it is fairly clear how to adjust our arguments to the weak case so that this obstacle is not a very serious one. Second, our arguments require that two successive evaluations of certain random variables be nearly independent. This requirement may be met by thinning out the time series, by, for example, using every tenth point encountered to calculate the series of distances used to estimate $C(r)$. Unfortunately, such a thinning, together with the required length of the surviving time series, amounts to restricting the validity of the error bounds we find to cases having extremely long time series, such as computer-modeled attractors. The third obstacle results from the need to bound the magnitude of $\left| E\left(\left(\frac{r}{\rho}\right)^p : r \leq \rho\right) - M(p) \right|$. In this article we make use of the very weak bound $\Delta_1 = A/a - a/A$, which, in addition, makes sense only when the relation $C(r) \sim r^d$ holds in the strong sense for which $a \leq C(r)/r^d \leq A$. What we need here is a stronger bound, especially one that is valid in the weak case. Finally, the fourth and most serious obstacle is posed by those correlation integrals $C(r)$ for which the limiting moment $M(p)$ does not exist (Theiler, 1988). As noted in section 2, the limiting moment *along an appropriate subsequence* $\rho_1, \rho_2, \rho_3, \dots$ still exists and yields the correlation dimension via (2.21), but the problem of extracting this subsequence is formidable.

An alternative approach would be to develop usable algorithms to enable us to decide when a specific attractor yields a strong case of the relation $C(r) \sim r^d$, not only to detect the strong case, but also to provide estimates of the associated parameters ρ_0 , A and a . For example, we may ask whether, for all practical cases, a numerical model of the Lorenz system (Lorenz, 1963) yields a strong case of the relation $C(r) \sim r^d$. Or, even more specifically, whether we may prove at least that the Smale-Williams hyperbolic attractor (Smale, 1977) yields a strong case, and if so, whether we may estimate rigorously values for the parameters ρ_0 , A and a . We suggest that such considerations as these may lead to an objective and effective algorithm to determine the scaling region in a computational or observational setting.

Application of our coarse relative error bound algorithm to the standard Henon attractor (Henon, 1976) yields values of the correlation dimension equal to $d_T = 1.25 \pm 0.15$ with probability 97.5% and moment error tolerance $\tau = 0.02$, and $d_T = 1.25 \pm 0.1$ with probability 90% and $\tau = 0.01$, respectively. These error bounds are similar to those reported in the literature (e.g., Simm *et al.*, 1987). Use of longer series to reduce noise contamination at small distances would presumably lead to improved estimates. If we are not interested in error bounds on the value of the dimension d , then our analysis suggests a simple procedure for estimating d from a time series of measurements. First we find several independent estimates d_a for d using the limiting moment $M(p)$. Upon plotting the approximate values of d as functions of the maximum distance ρ , we obtain a relatively small range of candidates d_T for d in an appropriate working interval of ρ . We determine the optimal value of d from this set of candidates by determining which one yields the smallest difference $A - a$ in the ratio $C(\rho)/\rho^{d_T}$ over the associated working interval of ρ . This approach is used by Fosmire (1993) in an analysis of two time series of atmospheric boundary layer winds.

The probabilistic context associated with our derivation leads to another method for generating the correlation function $C(r)$. Instead of using all the mutual distances between points on a relatively short time series of points on the attractor, we may use the distances between corresponding points on two extremely long time series. Because the two long time series pass through more of the attractor at a greater variety of scales, we may expect that the approximation to $C(r)$ thereby obtained is more accurate than the one obtained from the mutual distances in a short series. Of course the principal drawback to this technique is that it requires such a long time series that the method is effectively restricted to computer-modeled attractors.

Acknowledgments. We wish to thank Dr. Harry Henderson for his comments on an earlier draft of this manuscript. This research was supported by the Office of Naval Research through grant N00014-90-J-4012.

Appendix A

Completion of the Proof of the Statistical Error Estimate (5.14)

Our next task is to find an upper bound for the values of $\text{Var}(p, \rho)$ and $C(\rho) - C(\rho)^2$; we may combine (5.23) and (5.29) with the definition (5.32) to obtain

$$\text{Var}(p, \rho) \leq \left[\frac{A}{a} \frac{2p}{p+d} - \frac{a}{A} \frac{2p}{2p+d} - \frac{A^2}{a^2} \left(\frac{p}{p+d} \right)^2 \right] C(\rho) \quad (\text{A1})$$

We note in passing that the left side of (A1) is indeed positive. Using (A1), we may weaken (5.39) to the inequality

$$\begin{aligned} \text{Prob} \left(\left| M_0(p, \rho, n) - E((r/\rho)^p \chi(r/\rho)) \right| < \rho^{d+\delta} \quad \text{and} \quad |N(\rho, n)/n - C(\rho)| < \rho^{d+\delta} \right) \\ \geq 1 - \frac{C(\rho)}{\rho^{2d+2\delta} n} \left[\frac{A}{a} \frac{2p}{p+d} \right] - \frac{A}{\rho^{d+2\delta} n} - \frac{2\eta}{\rho^{2d+2\delta}} \end{aligned} \quad (\text{A2})$$

We check that the two premises

$$\left| M_0(p, \rho, n) - E((r/\rho)^p \chi(r/\rho)) \right| < \rho^{d+\delta} \quad (\text{A3})$$

and

$$|N(\rho, n)/n - C(\rho)| < \rho^{d+\delta} \quad (\text{A4})$$

imply the consecutive inequalities

$$\begin{aligned} \left| \frac{M_0(p, \rho, n)}{N(\rho, n)/n} - \frac{E((r/\rho)^p \chi(r/\rho))}{C(\rho)} \right| &\leq \frac{\rho^{d+\delta}}{N(\rho, n)/n} + \frac{E((r/\rho)^p \chi(r/\rho)) \rho^{d+\delta}}{C(\rho) N(\rho, n)/n} \\ &\leq \frac{\rho^{d+\delta}}{C(\rho) - \rho^{d+\delta}} + \frac{E((r/\rho)^p \chi(r/\rho)) \rho^{d+\delta}}{(C(\rho) - \rho^{d+\delta}) C(\rho)} \end{aligned} \quad (\text{A5})$$

where we have used (A4) in the second step. We note that the two equations

$$M(p, \rho, n) = \frac{M_0(p, \rho, n)}{N(p, \rho)/n} \quad (\text{A6})$$

$$E((r/\rho)^p : r \leq \rho) = \frac{E((r/\rho)^p \chi(r/\rho))}{C(\rho)}$$

follow from their definitions; further, we note that the trivial inequalities

$$E((r/\rho)^p \chi(r/\rho)) \leq C(\rho) \quad (\text{A7})$$

$$C(\rho) - \rho^{d+\delta} \geq (a - \rho^\delta) \rho^d$$

hold. Then we may use (A5)-(A7) to conclude that we have

$$\left| M(p, \rho, n) - E((r/\rho)^p : r \leq \rho) \right| \leq 2 \frac{\rho^\delta}{a - \rho^\delta} \quad (\text{A8})$$

Thus the conjunction of (A3) and (A4) implies (A8), and so the event described by (A3) and (A4) is contained in the event described by (A8). Consequently, we have

$$\text{Prob} \left(\left| M(p, \rho, n) - E((r/\rho)^p : r \leq \rho) \right| \leq 2 \frac{\rho^\delta}{a - \rho^\delta} \right) \geq \quad (\text{A9})$$

$$\text{Prob} \left(\left| M_0(p, \rho, n) - E((r/\rho)^p \chi(r/\rho)) \right| < \rho^{d+\delta} \quad \text{and} \quad \left| N(\rho, n)/n - C(\rho) \right| < \rho^{d+\delta} \right)$$

By combining (A9) and (A2), we obtain

$$\text{Prob} \left(\left| M(p, \rho, n) - E((r/\rho)^p : r \leq \rho) \right| \leq 2 \frac{\rho^\delta}{a - \rho^\delta} \right) \geq 1 - \frac{1}{\rho^{d+2\delta} n} \left(\frac{A^2}{a} \frac{2p}{p+d} + A \right) - \frac{2\eta}{\rho^{2d+2\delta}} \quad (\text{A10})$$

For values of ρ^δ satisfying $0 \leq \rho^\delta \leq a/21$, we have

$$2 \frac{\rho^\delta}{a - \rho^\delta} \leq \frac{2.1}{a} \rho^\delta \quad (\text{A11})$$

Making an obvious simplification on the right side of (A10), we then obtain, for small values of ρ ,

$$\text{Prob}\left(\left|M(p, \rho, n) - E\left((r/\rho)^p : r \leq \rho\right)\right| \leq \frac{2.1}{a} \rho^\delta\right) \geq 1 - \frac{2A^2 + Aa}{a\rho^{d+2\delta}n} - \frac{2\eta}{\rho^{2d+2\delta}} \quad (\text{A12})$$

Finally, we may rewrite (A12) using the abbreviation $\tau = 2.1\rho^\delta/a$ to obtain

$$\text{Prob}\left(\left|M(p, \rho, n) - E\left((r/\rho)^p : r \leq \rho\right)\right| \leq \tau\right) \geq 1 - \frac{40}{9} \frac{2A^2 + Aa}{a^3 \rho^d \tau^2 n} - \frac{2\eta}{\rho^{2d+2\delta}} \quad (\text{A13})$$

that is valid for $0 \leq \tau \leq \frac{1}{10}$. Equivalently, we have

$$\text{Prob}\left(\left|M(p, \rho, n) - E\left((r/\rho)^p : r \leq \rho\right)\right| > \tau\right) \leq \frac{40}{9} \frac{2A^2 + Aa}{a^3 \rho^d \tau^2 n} + \frac{2\eta}{\rho^{2d+2\delta}} \quad (\text{A14})$$

Thus, we arrive at the following probability estimate:

Statistical Error Estimate If the conditions $0 \leq \tau \leq \frac{1}{10}$ and (5.16), which is $n \geq 40(2A^2 + Aa)/(9\phi\rho^d a^3 \tau^2)$, hold, then we have

$$\text{Prob}\left(\left|M(p, \rho, n) - E\left((r/\rho)^p : r \leq \rho\right)\right| \leq \tau\right) \geq 1 - \phi \quad (\text{A15})$$

or, more precisely

$$\text{Prob}\left(\left|M(p, \rho, n) - E\left((r/\rho)^p : r \leq \rho\right)\right| \leq \tau\right) \geq 1 - \phi - \frac{80}{9} \frac{\eta}{\rho^{2d} \tau^2 a^2} \quad (\text{A16})$$

where η is the deviation from independence in (5.31).

Appendix B

Completion of the Proof of the Dimension Relative Error Bound (5.17)

We begin by noting that, from (2.18) we have $M(p) = d/(p+d)$, so that we may rewrite (5.13) as

$$\left| E\left(\left(\frac{r}{\rho}\right)^p : r \leq \rho\right) - M(p) \right| \leq \Delta_1 (1 - M(p)) \quad (\text{B1})$$

where we have introduced the abbreviation (5.19). Using (B1), we see, first, that

$$M(p) \geq \frac{E\left(\left(\frac{r}{\rho}\right)^p : r \leq \rho\right) - \Delta_1}{1 - \Delta_1} \quad (\text{B2})$$

and then that

$$\left| E\left(\left(\frac{r}{\rho}\right)^p : r \leq \rho\right) - M(p) \right| \leq \frac{\Delta_1}{1 - \Delta_1} [1 - E\left(\left(\frac{r}{\rho}\right)^p : r \leq \rho\right)] \quad (\text{B3})$$

hold. From (A16), we have that

$$\left| M(p, \rho, n) - E\left(\left(\frac{r}{\rho}\right)^p : r \leq \rho\right) \right| \leq \tau \quad (\text{B4})$$

holds with probability greater than or equal to $1 - \varphi - 80\eta/9\rho^{2d} \tau^2 a^2$ provided that (5.16) holds. Then we obtain from (B3) and (B4),

$$\left| M(p, \rho, n) - M(p) \right| \leq \frac{\Delta_1}{1 - \Delta_1} (\tau + 1 - M(p, \rho, n)) + \tau \quad (\text{B5})$$

which holds with probability greater than or equal to $1 - \varphi - 80\eta/9\rho^{2d} \tau^2 a^2$ provided that $n \geq n(\rho, \tau, \varphi)$ in (5.16).

We next compare the actual dimension d given by (2.6) with the approximate dimension d_a given by (5.12) that is obtained from our approximate moment $M(p, \rho, n)$ (5.11). In our calculation below, we also use

$$\frac{1-M(p)}{1-E((r/\rho)^p:r \leq \rho)} \leq \frac{1}{1-\Delta_1} \quad (\text{B6})$$

that follows immediately from (B1). Then we combine (B1), (B5), and (B6) to obtain

$$\left| \frac{d-d_a}{d} \right| \leq \frac{\Delta_1(1-M(p, \rho, n)) + \tau}{(1-M(p, \rho, n))(M(p, \rho, n) - \Delta_1 - \tau)} \quad (\text{B7})$$

Next we solve (5.12) for $M(p, \rho, n)$ and insert the result in (B7) to obtain finally our basic inequality

$$\left| \frac{d-d_a}{d} \right| \leq \frac{\Delta_1 p + \tau(p+d_a)}{d_a - (p+d_a)(\Delta_1 + \tau)} \frac{p+d_a}{p} = \varepsilon(\Delta_1, \tau, p, d_a) \quad (\text{B8})$$

bounding the error $|d-d_a|$ as a proportion of the actual dimension d , where the expression on the right side is the bound $\varepsilon(\Delta_1, \tau, p, d_a)$, (5.18), we seek. We note that similar maneuvers lead to a bound on the error as a proportion of the known quantity d_a ,

$$\left| \frac{d-d_a}{d_a} \right| \leq \frac{\Delta_1 p + \tau(p+d_a)}{p - \tau(p+d_a)} \frac{p+d_a}{d_a} \quad (\text{B9})$$

The bound (B8) is estimated in section 6 for the Henon attractor.

References

- Abraham, N. B., A. M. Albano, B. Das, G. DeGuzman, S. Yong, R. S. Goggia, G. P. Puccione and J. R. Tredicce, 1986: Calculating the dimension of attractors for small data sets. *Phys. Lett. A*, **114**, 217-221.
- Albano, A. M., J. Muench, C. Schwartz, A. I. Mees, and P. E. Rapp, 1988: Singular-value decomposition and the Grassberger-Procaccia algorithm. *Phys. Rev. A*, **38**, 3017-3026.
- Albano, A. M., A. Passamante, and M. E. Farrell, 1991: Using higher-order correlations to define an embedding window. *Physica*, **54D**, 85-97.
- Arneodo, A., G. Grasseau, and E. J. Kostelich, 1987: Fractal dimensions and $f(\alpha)$ spectrum of the Hénon attractor, *Phys. Lett. A*, **124**, 426-432.
- Baker, G. L. and J. P. Gollub, 1990: *Chaotic Dynamics: An Introduction*. Cambridge University Press, Cambridge, 182 pp.
- Barnsley, M. 1988: *Fractals Everywhere*. Academic Press, New York, 394 pp.
- Ben-Mizrachi, A., I. Procaccia, and P. Grassberger, 1984: Characterization of experimental (noisy) strange attractors. *Phys. Rev. A*, **29**, 975-977.
- Broomhead, D. S. and G. P. King, 1986: Extracting qualitative dynamics from experimental data. *Physica*, **20D**, 217-236.
- Caswell, W. E. and J. A. Yorke, 1986: Invisible errors in dimension calculations: Geometric and systematic effects. In *Dimensions and Entropies in Chaotic Systems—Quantification of Complex Behavior*, pp. 123-136, Mayer-Kress, G. (Ed.). *Springer Series in Synergetics*, **32**, Springer-Verlag, Berlin.
- Cutler, C. D., 1991: Some results on the behavior and estimation of the fractal dimensions of distributions on attractors. *J. Stat Phys.*, **62**, 651-708.
- Denker, M. and G. Keller, 1986: Rigorous statistical procedures for data from dynamical systems. *J. Stat. Phys.*, **44**, 67-93.
- Eckmann, J.-P. and D. Ruelle, 1985: Ergodic theory of chaos and strange attractors. *Rev. Mod. Phys.*, **57**, 617-656.
- Essex C., 1991: Correlation dimension and data sample size. In *Non-linear Variability in Geophysics*, pp. 93-98, D. Schertzer and S. Lovejoy (Eds.). Kluwer Academic Publishers, Dordrecht.

- Essex C., T. Lookman, and M. A. H. Nerenberg, 1987: The climate attractor over short time scales. *Nature*, **326**, 64-66.
- Essex, C. and M. A. H. Nerenberg, 1991: Comments on 'Deterministic chaos: the science and the fiction' by D. Ruelle. *Proc. Roy. Soc. Lond. A*, **435**, 287-292.
- Feller, W., 1957: *An Introduction to Probability Theory and Its Applications*, Volume 1, Second Edition. Wiley and Sons, New York, 461 pp.
- Feller, W., 1966: *An Introduction to Probability Theory and Its Applications*, Volume 2. Wiley and Sons, New York, 636 pp.
- Folland, G. B., 1984: *Real Analysis: Modern Techniques and Their Applications*. Wiley and Sons, New York, 350 pp.
- Fosmire, C. J., 1993: Estimating the correlation dimension of observed boundary layer winds. MS Thesis, The Pennsylvania State University (in preparation).
- Fraedrich, K., 1986: Estimating the dimensions of weather and climate attractors. *J. Atmos. Sci.*, **43**, 419-432.
- Franaszek, M., 1984: Effect of random noise on the deterministic chaos in a dissipative system. *Phys. Lett. A*, **105**, 383-386.
- Fraser, A. M. and H. L. Swinney, 1986: Independent coordinates for strange attractors from mutual information. *Phys. Rev. A*, **33**, 1134-1140.
- Grassberger, P., 1986: Do climate attractors exist? *Nature*, **323**, 609-612.
- Grassberger, P., 1987: Grassberger replies. *Nature*, **326**, 524.
- Grassberger, P., 1988: Finite sample corrections to entropy and dimension estimates. *Phys. Lett. A*, **128**, 369-373.
- Grassberger, P. and I. Procaccia, 1983a: Characterization of strange attractors. *Phys. Rev. Lett.*, **50**, 346-349.
- Grassberger, P. and I. Procaccia, 1983b: Measuring the strangeness of strange attractors. *Physica*, **9D**, 189-208.
- Greenside, H. S., A. Wolf, J. Swift, and T. Pignato, 1982: Impracticality of a box-counting algorithm for calculating the dimensionality of strange attractors. *Phys. Rev. A*, **25**, 3453-3456.
- Henderson, H. W. and R. Wells, 1988: Obtaining attractor dimensions from meteorological time series. *Adv. Geophys.*, **30**, 205-237.

- Henon, M., 1976: A two-dimensional mapping with a strange attractor. *Comm. Math. Phys.*, **50**, 69-77.
- Hentschel, H. G. E. and I. Procaccia, 1983: The infinite number of generalized dimensions of fractals and strange attractors. *Physica*, **8D**, 435-444.
- Holzfuss, J. and G. Mayer-Kress, 1986: An approach to error-estimation in the application of dimension algorithms. In *Dimensions and Entropies in Chaotic Systems—Quantification of Complex Behavior*, pp. 114-122, Mayer-Kress, G. (Ed.). *Springer Series in Synergetics*, **32**, Springer-Verlag, Berlin.
- James, R. C., 1967: *Advanced Calculus*. Wadsworth Publishing Company, Belmont, CA, 646 pp.
- Judd, K., 1992: An improved estimator of dimension and some comments on providing confidence intervals. *Physica*, **56D**, 216-228.
- Kaplan, J. L. and J. A. Yorke, 1979: Chaotic behavior of multidimensional difference equations. In *Functional Differential Equations and the Approximation of Fixed Points*, pp. 228-237, H. O. Peitgen and H. O. Walther (Eds.). *Lecture Notes in Mathematics*, **730**, Springer-Verlag, Berlin.
- Kember, G. and A. C. Fowler, 1992: Random sampling and the Grassberger-Procaccia algorithm. *Phys. Lett. A*, **161**, 429-432.
- Keppene, C. L. and C. Nicolis, 1989: Global properties and local structure of the weather attractor over Western Europe. *J. Atmos. Sci.*, **46**, 2356-2370.
- Lorenz, E. N., 1963: Deterministic nonperiodic flow. *J. Atmos. Sci.*, **20**, 130-141.
- Lorenz, E. N., 1991: Dimension of weather and climate attractors. *Nature*, **353**, 241-244.
- Mandelbrot, B., 1983: *The Fractal Geometry of Nature*. W. H. Freeman and Co., New York, 468 pp.
- Mañé, R., 1981: On the dimension of the compact invariant sets of certain nonlinear maps. In *Dynamical Systems and Turbulence, Warwick 1980*, pp. 230-242, D. A. Rand and L.-S. Young, (Eds.). *Lecture Notes in Mathematics*, **898**, Springer-Verlag, Berlin.
- Nerenberg, M. A. H. and C. Essex, 1990: Correlation dimension and systematic geometric effects. *Phys. Rev. A*, **42**, 7065-7074.
- Nerenberg, M. A. H., T. Lookman, and C. Essex, 1991: On the existence of low dimensional climatic attractors. In *Non-linear Variability in Geophysics*, pp. 251-255, D. Schertzer and S. Lovejoy (Eds.). Kluwer Academic Publishers, Dordrecht.

- Nese, J. M. 1987: Diagnosing the structures of attractors. In *Nonlinear Hydrodynamic Modeling: A Mathematical Introduction*, pp. 412-443, H. N. Shurer (Ed.), *Lecture Notes in Physics*, **271**, Springer-Verlag, Berlin.
- Nese, J. M., J. A. Dutton, and R. Wells, 1987: Calculated attractor dimensions for low-order spectral models. *J. Atmos. Sci.*, **44**, 1950-1972.
- Nicolis, C. and G. Nicolis, 1984: Is there a climate attractor? *Nature*, **311**, 529-532.
- Nicolis, C. and G. Nicolis, 1987: Evidence for climatic attractors. *Nature*, **326**, 523.
- Osborne, A. R. and A. Provenzale, 1989: Finite correlation dimension for stochastic systems with power-law spectra. *Physica*, **35D**, 357-381.
- Procaccia, I: 1988: Weather systems—complex or just complicated? *Nature*, **333**, 498-499.
- Ramsey, J. B. and H.-J. Yuan, 1989: Bias and error bars in dimension calculations and their evaluation in some simple models. *Phys. Lett. A*, **134**, 287-297.
- Ruelle, D., 1990: Deterministic chaos: the science and the fiction. *Proc. Roy. Soc. Lond. A*, **427**, 241-248.
- Russell, D. A., J. D. Hanson, and E. Ott, 1980: Dimension of strange attractors. *Phys. Rev. Lett.*, **45**, 1175-1178.
- Simm, C. W., M. L. Sawley, F. Skiff, and A. Pochelon, 1987: On the analysis of experimental signals for evidence of deterministic chaos. *Helvetica Physica Acta*, **60**, 510-551.
- Smale, S., 1977: Dynamical systems and turbulence. In *Turbulence Seminar, Berkeley 1976/77*, pp. 48-70, A. Dold and B. Eckmann (Eds.). *Lecture Notes in Mathematics*, **615**, Springer-Verlag, Heidelberg.
- Smith, L. A., 1988: Intrinsic limits on dimension calculations. *Phys. Lett. A*, **133**, 283-288.
- Smith, L. A., J.-D. Fournier, and E. A. Spiegel, 1986: Lacunarity and intermittency in fluid turbulence. *Phys. Lett. A*, **114**, 465-468.
- Takens, F., 1981: Detecting strange attractors in turbulence. In *Dynamical Systems and Turbulence, Warwick 1980*, pp. 366-381, D. A. Rand and L.-S. Young, (Eds.). *Lecture Notes in Mathematics*, **898**, Springer-Verlag, Berlin.

- Takens, F., 1985: On the numerical determination of the dimension of an attractor. In *Dynamical Systems and Bifurcations, Proceedings, Groningen 1984*, pp. 99-106, B. L. J. Braaksma, H. W. Broer, and F. Takens (Eds.). *Lecture Notes in Mathematics*, **1125**, Springer-Verlag, Berlin.
- Theiler, J. 1986: Spurious dimension from correlation algorithms applied to limited time-series data. *Phys. Rev. A*, **34**, 2427-2432.
- Theiler, J., 1987: Efficient algorithm for estimating the correlation dimension from a set of discrete points. *Phys. Rev. A*, **36**, 4456-4462.
- Theiler, J., 1988: Lacunarity in a best estimator of fractal dimension. *Phys. Lett. A*, **133**, 195-200.
- Theiler, J., 1990: Statistical precision of dimension estimators. *Phys. Rev. A*, **41**, 3038-3051.
- Theiler, J., 1991: Some comments on the correlation dimension of $1/f^\alpha$ noise. *Phys. Lett. A*, **155**, 480-493.
- Thomson, D. W. and H. W. Henderson, 1992: Definition of local atmospheric attractors using measurements made with surface-based remote sensing systems. *Proceedings of the First Experimental Chaos Conference*, pp. 389-402. World Scientific Publishing Co.
- Tsonis, A. A., 1992: *Chaos: From Theory to Applications*. Plenum, New York, 269 pp.
- Tsonis A. A. and J. B. Elsner, 1988: The weather attractor over very short time scales. *Nature*, **33**, 545-547.
- Tsonis A. A. and J. B. Elsner, 1989: Chaos, strange attractors, and weather. *Bull. Am Met. Soc.*, **70**, 14-23.
- Tsonis A. A. and J. B. Elsner, 1990: Comments on "Dimension analysis of climatic data". *J. Climate*, **3**, 1502-1505.
- Tsonis, A. A., J. B. Elsner, and K. P. Georgakakos, 1993: Estimating the dimension of weather and climate attractors: What do we know about the procedure and what do the results mean? Submitted to *J. Atmos. Sci.*